ating. However, if they are, the experimental results show that their relative contribution to the total diffusion coefficient cannot vary with temperature, because $1 - (D_{60}/D_{55})$ is temperature-independent. This is not likely for any of the possible second mechanisms. Hence, only one mechanism, the vacancy mechanism, is operating.

Ultraviolet Magneto-Optical Properties of Single-Crystal Orthoferrites, Garnets, and Other Ferric Oxide Compounds*†

FREDERIC J. KAHN‡ AND P. S. PERSHAN

Division of Engineering and Applied Physics, Harvard University, Cambridge, Massachusetts 02138

AND

J. P. REMEIKA

Bell Telephone Laboratories, Murray Hill, New Jersey 07974

(Received 1 April 1969)

The ultraviolet and visible linear magneto-optical properties of representative ferric oxide compounds were measured by reflection methods between 1.7 and 5.64 eV at room temperature. The experimental technique, based on the complex polar Kerr effect (rotation and ellipticity), was applied to all available single-crystal rare-earth orthoferrites and to representative rare-earth iron garnets, nickel spinel ferrite, and magnetoplumbite. For representative orthoferrites and yttrium iron garnet, the magneto-optical results were reduced, with the aid of additional straight (nonmagnetic) reflectivity data, to obtain the magnetically induced off-diagonal elements of the dielectric tensor. Presentation of the magneto-optical results in the form of the tensor elements facilitates comparison with microscopic theories because of the difference in energy dependence between the tensor elements and the experimental observables. The observed spectra are analyzed in terms of a molecular-orbital theory that elaborates on an earlier calculation by Clogston. For the orthoferrites, explicit calculation of the dielectric-tensor elements has made it possible to identify the most prominent features in the magneto-optical spectra in terms of explicit charge-transfer and crystal-field transitions. The magneto-optical effects in the orthoferrites are approximately the same order of magnitude as in the garnets, although a simple theory would have them an order of magnitude smaller. This is interpreted as evidence for an anisotropic orbital quenching that follows from the low symmetry of the Fe ion in the orthoferrites. Magneto-optical measurements on gallium-substituted europium iron garnet has made it possible to differentiate between the magneto-optical structure that arises from Fe ions on octahedral and tetrahedral sites.

I. INTRODUCTION

A. Motivation and Scope

ALTHOUGH the ferric oxide compounds have been extensively studied, relatively little is known about the wave functions of the electrons that bind them and are responsible for their magnetic character. Much of our present knowledge is restricted to phenomenological constants that describe the material properties without really explaining their origin. The essential information, a knowledge of the actual wave functions of the magnetic ions, is for the most part lacking. Contribution to this essential knowledge is the objective of the present investigation.

Through the use of optical and magneto-optical (complex polar Kerr effect) reflection techniques, we have made observations of the ultraviolet spectra of bulk, single-crystal ferric oxide compounds.[1,2] The lack of experimental data has for the most part restricted previous workers to speculation on the nature of the highly absorbing transitions which render these materials opaque. The experimental results of the present investigation provide a firm basis for the evaluation of microscopic models and the identification of individual electronic transitions.

[1] F. J. Kahn, P. S. Pershan, and J. P. Remeika, Phys. Rev. Letters **21**, 804 (1968).

[2] F. J. Kahn, P. S. Pershan, and J. P. Remeika, J. Appl. Phys. **40**, 1508 (1969).

To our knowledge there have been no previous measurements of the complex polar Kerr effect in the ultraviolet. Although we have chosen to apply these techniques to studies of the ferric oxide compounds, the methods employed are generally applicable. In Sec. VI we suggest additional classes of materials for which we feel similar measurements would be profitable.

The high-sensitivity Kerr spectrometer designed and constructed for this investigation is simultaneously more sensitive and more versatile than any previous spectrometer that we know of for magneto-optical reflection measurements. It accurately measures small magneto-optical effects produced by reflection from small samples over an extended wavelength range. The magneto-optical measurement techniques and apparatus will be described elsewhere.[3]

B. Previous Investigations

1. Precursor Studies

When Morin[4] studied the transmission of α-Fe_2O_3 in 1954, the rare-earth iron garnets had already been grown by the French, but they were not actually identified until 1956 when Bertaut, Forrat, Néel, and Pauthenet announced this new category of ferrimagnetic materials.[5,6] Soon afterwards, in 1957, Geller and Gilleo,[5,7] who had independently discovered the rare-earth iron garnets, presented the results of their experiments.

The optical properties of these new materials were studied in transmission by Dillon, who observed large Faraday rotations associated with a strong visible absorption edge,[8] thereby stimulating considerable interest in the optical and magneto-optical properties of ferric oxide compounds.[9–18] Clogston discussed the

phenomena observed by Dillon in terms of electric-dipole-allowed transitions, i.e., charge transfer and orbital promotion.[9] However, the strength of these transitions and the resulting opaqueness of these materials has, to the present time, prevented confirmation or elaboration of his theories. Note that transmission experiments are not possible at energies above 2.5 eV ($\approx 20\,000$ cm^{-1}) for even the thinnest sections which have been prepared from bulk single crystals of undiluted ferric oxide compounds.

2. Previous Experimental Studies

Grant has independently measured the straight reflectivity of yttrium and gadolinium iron garnets.[17] Magneto-optical measurements, however, convey considerably more information than straight reflectivity. The previous magneto-optical studies of ferric oxide compounds mentioned above were limited either to the visible range[8,10,11,13,15] or to Faraday rotation of polycrystalline films.[14,18]

The off-diagonal elements of the dielectric tensor, necessary for comparison of the magneto-optical spectra with microscopic theory, were obtained only by Jung, who studied erbium orthoferrite in the visible.[15] Jung derived the off-diagonal elements by application of Kramers-Kronig relations that are only valid for regions of weak absorption.[19] Nevertheless, since Jung's results are for the visible and therefore do not refer to the most strongly absorbing regions, they have a qualitative resemblance to the elements derived in the present investigation. The present results, however, are valid for all regions—weakly or strongly absorbing.

A different experimental approach to uv magneto-optics is that of Krinchik and Artemjev, who have applied the transverse Kerr effect to the study of iron, nickel, and cobalt metals between 0.2 and 6 eV.[20] We note here, only in passing, that the complex polar Kerr technique has definite advantages over the transverse method for the purposes of the present investigation.[3]

3. Previous Theory and Interpretation

The earliest and most detailed theories relevant to the current investigation are those of Clogston,[9] who reasoned that the large magneto-optical effects and strong absorptions observed in the rare-earth iron garnets could only be accounted for by the large oscillator strengths of electric-dipole-allowed transitions. He argued that either charge-transfer excitations ($^6A_{1g}\rightarrow{}^6T_{1u}$) or orbital promotion excitations ($^6S\rightarrow{}^6P$) could explain the observed transmission spectra. In addition, he attributed the relatively weak but sharp peaks observed in the garnet transmission spectra to spin- and parity-forbidden crystal-field transitions whose intensities are enhanced by admixture with allowed orbital-promotion excitations.

[3] F. J. Kahn (to be published). See also F. J. Kahn, Ph.D. thesis, Harvard University, 1968 (unpublished), available in Xerox or microfilm form from Archives, Widener Library, Harvard, or in technical report form from Defense Documentation Center.

[4] F. J. Morin, Phys. Rev. 93, 1195 (1954).

[5] B. Lax and K. L. Button, Microwave Ferrites and Ferrimagnetics (McGraw-Hill Book Co., New York, 1962), Chap. 1.

[6] L. Néel, R. Pauthenet, and B. Dreyfus, Progr. Low Temp. Phys. 4, 344 (1964).

[7] S. Geller, Z. Krist. 125, 1 (1967).

[8] J. F. Dillon, Jr., J. Phys. Radium 20, 374 (1959), and references cited therein.

[9] A. M. Clogston, J. Phys. Radium 20, 151 (1959); J. Appl. Phys. 31, 198S (1960).

[10] R. C. Sherwood, J. P. Remeika, and H. J. Williams, J. Appl. Phys. 30, 217 (1959).

[11] P. C. Bailey, J. Appl. Phys. 31, 39S (1960); P. C. Bailey and A. Goldman, Westinghouse Research Laboratories Final Report No. AF19(609)-5529, 1960 (unpublished).

[12] K. A. Wickersheim and R. A. Lefever, J. Chem. Phys. 36, 844 (1962).

[13] C. A. Fowler, Jr., E. M. Fryer, B. L. Brandt, and R. A. Isaacson, J. Appl. Phys. 34, 2064 (1963).

[14] R. L. Coren and M. H. Francombe, J. Phys. Radium 25, 233 (1964).

[15] W. Jung, J. Appl. Phys. 36, 1249 (1965).

[16] D. L. Wood and J. P. Remeika, J. Appl. Phys. 38, 1038 (1967).

[17] P. M. Grant, Appl. Phys. Letters 11, 166 (1967).

[18] R. E. MacDonald, O. Voegeli, and C. D. Mee, J. Appl. Phys. 38, 4101 (1967).

[19] W. Jung (private communication).

[20] G. S. Krinchik and V. S. Artemjev, J. Appl. Phys. 39, 1276 (1968), and references cited therein.

Wickersheim and Lefever[12] discounted the importance of orbital promotion in the region of the absorption edge and attributed the strong continuous absorption above 20 000 cm^{-1} to charge-transfer processes. These authors also introduced the use of reduced term separations to explain the energies of absorptions attributed to crystal-field transitions.

Jung attributed the principal features of his visible spectra for erbium orthoferrite to charge-transfer transitions and noted that another strong band at higher energy must contribute a large portion of the dielectric constant which he observed in the visible.[15] These observations of Jung are supported by the results of the present investigation. However, his additional speculations, in which he attempted to identify the charge-transfer and higher-energy transitions and to interpret the dispersion of the off-diagonal elements of the dielectric tensor, are not supported by the present results. Jung lacked two important types of information—the uv spectra which we present in Sec. III and the lines-shape theory given in Sec. V—results that are of crucial importance in the determination of spectral assignments.

The p-type photoconductivity which Grant observed in gadolinium iron garnet can be interpreted as resulting from charge-transfer processes.[21] In addition, Grant attributes the structure in his reflectivity spectra to charge-transfer-enhanced crystal-field transitions superposed on a broad charge-transfer background.[17] Instead of attempting definite assignments, he points out that the observed reflection peaks correlate with the crystal-field transition energies computed by Wood and Remeika.[16] The latter are based on additional refinements to the fitting procedure of Wickersheim and Lefever.[12] The spectra attributed to charge-transfer-enhanced crystal-field transitions in the current investigation also correlate with the results of Wood and Remeika. However, the magneto-optical methods employed enable us to further identify the charge-transfer transitions as well.

C. Outline

The macroscopic theory of the complex polar Kerr effect is given in Sec. II. Experimental results are presented in Sec. III for the weakly ferromagnetic rare-earth orthoferrities, the simplest ferric oxide compounds from the perspective of the present investigation. Results for the ferrimagnetic ferric oxide compounds, including the rare-earth iron garnets, are given in Sec. IV. The experimental spectra are analyzed in Sec. V in terms of a molecular-orbital theory that is an elaboration of the proposals of Clogston. The concluding section suggests some possible areas for future research which are a consequence of the current investigation.

[21] P. M. Grant and W. Ruppel, Solid State Commun. **5**, 543 (1967).

II. MACROSCOPIC THEORY

A. Introduction

In the polar Kerr geometry, an external magnetic field is applied normal to the sample surface in order to align the sample magnetization. Plane-polarized light is then reflected at normal incidence with a slightly rotated and slightly elliptical polarization. The complex polar Kerr effect is then defined by

$$\Phi = \varphi + i\theta, \qquad (1)$$

where φ is the rotation of the plane of polarization of the reflected beam with respect to that of the incident beam and θ is the ellipticity which must be associated with this rotation as a consequence of causality. That is, φ is the angle between the original plane of polarization and the plane of the principal axis of the elliptically polarized reflected beam and $\tan\theta$ is the ratio of the minor to major axes of the ellipse that describes the polarization of the reflected beam.

B. Normal Modes and Dielectric Tensor

At optical frequencies the propagation of electromagnetic waves may be fully described by a delectric tensor ε.[22] For $\mathbf{M}\|\hat{z}$, this tensor is of the form[22,23]

$$\varepsilon = \begin{bmatrix} \epsilon_0+\epsilon_2 & +i\epsilon_1 & 0 \\ -i\epsilon_1 & \epsilon_0-\epsilon_2 & 0 \\ 0 & 0 & \epsilon_z \end{bmatrix}, \qquad (2)$$

where the cordinate axes have been taken to lie along the principal axes of the crystal.

To first order in the magnetization, the tensor elements are independent of $\mathbf{M}$, except for ϵ_1, which is linear in $\mathbf{M}$. For an absorbing medium they are complex and given by $\epsilon_j = \epsilon_j' + i\epsilon_j''$. We assume the convention that field quantities propagate as $e^{i(\mathbf{k}\cdot\mathbf{r}-\omega t)}$. Birefringence and pleochroism, which have been accounted for by ϵ_2, will be zero for a crystal with an axis along $\hat{z}$ that has threefold or higher symmetry.

Diagonalization of ε gives the normal modes of propagation for $\mathbf{k}\|\hat{z}$. These modes, corresponding to the eigenvalues

$$n_{\pm}^2 = \epsilon_0 \pm (\epsilon_1^2 + \epsilon_2^2)^{1/2}, \qquad (3)$$

have eigenvectors, describing the polarization, that may be written in the form

$$\hat{r}_+ = -ib\hat{x} + a\hat{y}, \quad \hat{r}_- = a\hat{x} - ib\hat{y}, \qquad (4)$$

where a and b are functions of ϵ_0, ϵ_1, and ϵ_2. In general,

$$\hat{r}_+ \cdot \hat{r}_-^* = \hat{r}_- \cdot \hat{r}_+^* = i\gamma \qquad (5)$$

is unequal to zero; therefore the normal modes are not generally orthogonal. Orthogonal modes are obtained

[22] L. D. Landau and E. M. Lifshitz, *Electrodynamics of Continuous Media* (Pergamon Press, Ltd., London, 1960); see also P. S. Pershan, J. Appl. Phys. **38**, 1482 (1967).

[23] L. D. Landau and E. M. Lifshitz, *Statistical Physics* (Pergamon Press, Ltd., London, 1958), pp. 379–406.

only for $\gamma=0$, a condition which is satisfied when either $\epsilon_1=0$, $\epsilon_2=0$, or ϵ_1'' and ϵ_2'' equal zero. Note that $\boldsymbol{\epsilon}$ need not be Hermitian for the normal modes to be orthogonal. For $\epsilon_1=0$, the normal modes are linearly polarized, whereas for $\epsilon_2=0$, they are circularly polarized. For the general case, a full range of elliptical modes is obtained with eccentricities depending on the relative values of ϵ_1 and ϵ_2.

C. Complex Polar Kerr Effect

1. Nonpleochroic Media $(\epsilon_2=0)$

Decomposition of the incident beam into the normal modes of Eq. (4) enables us to compute the complex polar Kerr rotation. For $\epsilon_2=0$, Φ is given in terms of the tensor elements by[24]

$$\Phi = -i\epsilon_1/\epsilon_0^{1/2}(\epsilon_0-1).\quad(6)$$

If the sample magnetization is taken to be positive when it points in the direction of propagation of the reflected beam, Eq. (6) will be consistent with the standard sign convention.[25] As applied to the present investigation, this convention states that a rotation in the direction of the current that produces the magnetic field used to align the sample's magnetization will be positive. Equation (6) is used to analyze the experimental data presented in Secs. III and IV, and the signs of the data are given according to the above convention. Analysis of expressions analogous to Eq. (6) but for non-normally incident beams[24,26] shows that for angles of incidence as large as 15° the main effect of non-normal incidence (taking $|\epsilon_0|\sim 6$) is merely to reduce the observed Kerr rotation by a few percent. Thus measurements of the polar Kerr effect need not be made in the inconvenient normal incidence geometry.

For a transmission experiment, the expression analogous to Eq. (6) is

$$\Phi_T = -\pi(L/\lambda)(\epsilon_1/\epsilon_0^{1/2}),\quad(7)$$

where L is the optical path length, λ is the wavelength in free space, and $\mathbf{M}$ is taken to be positive in the direction of propagation. Comparing Eqs. (6) and (7), we see that the magneto-optical reflection effects may be considered to arise from an effective path length

$$L_{\text{eff}} \approx (\lambda/\pi)|\epsilon_0-1|^{-1}.\quad(8)$$

Thus transmission effects will be considerably larger than reflection effects for materials sufficiently transparent to transmit light through a path of one of more wavelengths. However, in strongly absorbing materials for which transmission measurements must be made on thin films, the transmission and reflection effects will be of comparable magnitude.

[24] N. Voigt, *Magneto- und Elektrooptik* (B. G. Teubner, Leipzig, 1908).

[25] R. W. Ditchburn, *Light* (Wiley-Interscience Inc., New York, 1958), p. 527.

[26] E. A. Stern, J. C. McGroddy, and W. E. Harte, Phys. Rev. **135A**, 1306 (1964).

2. Pleochroic Media $(\epsilon_2\neq 0)$

Determination of Φ for the general case ϵ_1, $\epsilon_2\neq 0$ involves considerable algebra and results in very complicated expressions due to the nonorthogonality of the normal modes. However, the expressions for the general case provide important information and to our knowledge have not previously been published. Their derivation is given in the Appendix. The results of this derivation are quoted here.

We consider a beam of linearly polarized monochromatic light normally incident on a crystal represented by $\boldsymbol{\epsilon}$ of Eq. (2). The beam, polarized at angle α measured counterclockwise from $\hat{x}$, is given by

$$\mathbf{E}_{\text{in}} = E_0(\hat{x}\cos\alpha+\hat{y}\sin\alpha).\quad(9)$$

The complex polar Kerr rotation on reflection from the crystal is

$$\Phi = [\mu/(1+\gamma^2)]\{[i\gamma(aa^*-bb^*)-i(ab^*+a^*b)]\\-[(aa^*-bb^*)+\gamma(ab^*+ba^*)]\sin2\alpha\}\quad(10)$$

to first order in ϵ_1/ϵ_0 and ϵ_2/ϵ_0, where

$$\mu = \frac{(\epsilon_1^2+\epsilon_2^2)^{1/2}}{\epsilon_0^{1/2}(1-\epsilon_0)} \approx \frac{n_+-n_-}{1-\epsilon_0},\quad(11)$$

and the remaining quantities are as defined in Eqs. (4) and (5).

The origins of the various terms in Eq. (10) are determined by tracing through the derivation. If we consider ϵ_1 and ϵ_2 to be perturbations on an isotropic medium, the factor μ arises from the difference in eigenvalues, n_+-n_-, of the perturbed modes. The terms within the parentheses result from the perturbation of the eigenmodes themselves. Furthermore, one of these eigenmode terms depends on $\sin2\alpha$ and the other does not. The term in $\sin2\alpha$ describes the pleochroic and birefringent effects associated with ϵ_2; the term independent of α describes the magneto-optical effects associated with ϵ_1.

The two limiting cases for Eq. (10) are $|\epsilon_1|\gg|\epsilon_2|$ and $|\epsilon_1|\ll|\epsilon_2|$. For $|\epsilon_1|\gg|\epsilon_2|$ we expect to get the result of Eq. (6), which was derived for $\epsilon_2=0$, plus an additional term dependent on $\sin2\alpha$. For both cases, $|\epsilon_1|\gg|\epsilon_2|$ and $|\epsilon_1|\ll|\epsilon_2|$, we find to first order in ϵ_1/ϵ_0 and ϵ_2/ϵ_0

$$\Phi \approx -\frac{i\epsilon_1+\epsilon_2\sin2\alpha}{\epsilon_0^{1/2}(\epsilon_0-1)}.\quad(12)$$

A common error that frequently enters discussions of these phenomena is that for $|\epsilon_2|\gg|\epsilon_1|$, no linear—and hence no appreciable—magneto-optical effects can be observed. However, Eq. (12) shows for reflection measurements that the anisotropy due to ϵ_2 does not quench the linear effects in either limiting case. The physical reason is that the effective path length for reflection is too small for birefringence or pleochroism to quench the linear magneto-optical effects.

Since ϵ_1 is linear in $\mathbf{M}$ while ϵ_2 is independent of $\mathbf{M}$, the magneto-optical part of Φ can be measured independently of ϵ_2. For the case $|\epsilon_1| \gg |\epsilon_2|$, the linear magneto-optical effect arises from the difference in the eigenvalues of the perturbed modes. For $|\epsilon_2| \gg |\epsilon_1|$ the difference in the eigenvalues will no longer be linear in ϵ_1, the linear term having been quenched by ϵ_2. However, the eigenmodes are also perturbed and in this case their perturbation gives rise to terms linear in ϵ_1 which result in the linear magneto-optical effect of Eq. (12).

In transmission measurements, a linear magneto-optical effect for the case $|\epsilon_1| \ll |\epsilon_2|$ can be similarly demonstrated. The analog of Eq. (10) for transmission is

$$\tan\Phi_T = [(\tan\nu)/(a^2+b^2)][2ab+i(b^2-a^2)\sin2\alpha] \quad (13)$$

to first order in ϵ_1/ϵ_0 and ϵ_2/ϵ_0, where

$$\nu = (\epsilon_1{}^2+\epsilon_2{}^2)^{1/2}k_0L/2\epsilon_0{}^{1/2}, \quad (14)$$

and for simplicity $\boldsymbol{\varepsilon}$ has been assumed to be real. For $\epsilon_1=0$, ν is the maximum rotation due to birefringence.

For sufficiently short path lengths or sufficiently small birefringences and ϵ_1, $\nu \ll 1$ and $\tan\nu \approx \nu$. We can then show that for either $|\epsilon_1| \gg |\epsilon_2|$ or $|\epsilon_1| \ll |\epsilon_2|$,

$$\Phi_T = -\frac{\pi L}{\lambda}\left(\frac{\epsilon_1 - i\epsilon_2\sin2\alpha}{\epsilon_0{}^{1/2}}\right) \quad (15)$$

to first order in ϵ_1/ϵ_0 and ϵ_2/ϵ_0, a result for transmission analogous to Eq. (12) in both form and explanation. For $|\epsilon_1| \ll |\epsilon_2|$, the condition $\nu \ll 1$ for the existence of linear magneto-optical effects in transmission is found from Eq. (14) to be

$$\pi(\epsilon_1{}^2+\epsilon_2{}^2)^{1/2}L \ll \epsilon_0{}^{1/2}\lambda. \quad (16)$$

Note that for highly absorbing materials transmission measurements must be made on thin films and Eq. (16) will be satisfied. Also note that for $|\epsilon_1| \gg |\epsilon_2|$ we obtain

$$\tan\Phi_T = (\tan\nu)[-1+i(\epsilon_2/\epsilon_1)\sin2\alpha] \quad (17)$$

to first order in ϵ_1/ϵ_0 and ϵ_2/ϵ_0, independently of whether Eq. (16) is satisfied.

D. Dispersion Relations

If the spectral components $\mathbf{D}(\omega)$ and $\mathbf{E}(\omega)$ of two physically real observables $\mathbf{D}(t)$ and $\mathbf{E}(t)$ are linearly related by

$$\mathbf{D}(\omega) = \boldsymbol{\varepsilon}(\omega) \cdot \mathbf{E}(\omega), \quad (18)$$

and $\mathbf{E}(t)$ causes $\mathbf{D}(t)$, then the real and imaginary parts of $\boldsymbol{\varepsilon}$ will satisfy Kramers-Kronig relations.[27] In the present investigation, we make the identifications of $\mathbf{D}$ with electric displacement, $\mathbf{E}$ with electric field, and $\boldsymbol{\varepsilon}$ with the dielectric tensor. The Kramers-Kronig relations are applicable to all components of the dielectric tensor $\boldsymbol{\varepsilon}$ and can be used to calculate $\epsilon_j{}'$ or

$\epsilon_j{}''$ when only one is known over a broad range of frequencies. As a result of explicit frequency dependences in the integrands of these relations, the major contribution to $\epsilon_j{}'$ ($\epsilon_j{}''$) are from spectral components of the first derivative of $\epsilon_j{}''$ ($-\epsilon_j{}'$) lying nearby in frequency. The extrema of $\epsilon_j{}'$ and $\epsilon_j{}''$ therefore have the following correlations in frequency:

$$\begin{pmatrix} \epsilon_j{}'_{\max} \\ \epsilon_j{}'_{\min} \end{pmatrix} \leftrightarrow \begin{pmatrix} (d\epsilon_j{}''/d\omega)_{\max} \\ (d\epsilon_j{}''/d\omega)_{\min} \end{pmatrix},$$

$$\begin{pmatrix} \epsilon_j{}''_{\max} \\ \epsilon_j{}''_{\min} \end{pmatrix} \leftrightarrow \begin{pmatrix} (d\epsilon_j{}'/d\omega)_{\min} \\ (d\epsilon_j{}'/d\omega)_{\max} \end{pmatrix}. \quad (19)$$

The off-diagonal element ϵ_1, defined in Eq. (2), satisfies the conditions for the Kramers-Kronig relations, and its real and imaginary parts therefore have the correlations given by Eq. (19). However, the polar Kerr rotation φ and the polar Kerr ellipticity θ were shown in Eq. (6) to consist of linear combinations of $\epsilon_1{}'$ and $\epsilon_1{}''$ determined by a function of ϵ_0. Since ϵ_0 is frequency-dependent φ and θ themselves do not satisfy Kramers-Kronig relations of the standard form.

Equation (19) provides a check on the self-consistency of the tensor elements computed from the experimental spectra to be presented in Secs. III and IV. Another application of dispersion relations in the current investigation is the determination of the diagonal elements ϵ_0 from the normal reflectivity R measured over a broad frequency range. This method for determining ϵ_0 is discussed in the literature by Stern,[27] Toll,[28] and others.

III. RARE-EARTH ORTHOFERRITES

A. Physical Properties

The rare-earth orthoferrities formula $R\mathrm{FeO}_3$ and space group $D_{2h}{}^{16}\text{-}Pbnm$ have a distorted perovskite structure with only one type of Fe^{3+} ion, Fe^{3+} octahedrally coordinated with O^{2-} ions.[29,30] There are four Fe^{3+} ions, with $\bar{1}$ point symmetry, per orthorhombic unit cell. These ions are related by the space-group operations. In the microscopic theory of Sec. V, the large linear magneto-optical effects observed in the orthoferrites are attributed to the low point symmetry

The magnetic properties of the orthoferrites have been summarized by White,[31] Treves,[32] and the references therein. The basic magnetic interaction is antiferromagnetic between nearest-neighbor Fe^{3+} ions. A slight canting of the Fe^{3+} spins, due to antisymmetric exchange, produces a weak net magnetization $4\pi\mathbf{M}$ on the order of 100 G at room temperature. The rare-earth ions, at room temperature, behave like paramagnets in

---

[27] F. Stern, Solid State Phys. **15**, 327 (1963).

[28] J. S. Toll, Phys. Rev. **104**, 1760 (1956).
[29] S. Geller and E. A. Wood, Acta Cryst. **9**, 563 (1956).
[30] S. Geller, J. Chem. Phys. **24**, 1236 (1956).
[31] R. L. White, J. Appl. Phys. **40**, 1061 (1969).
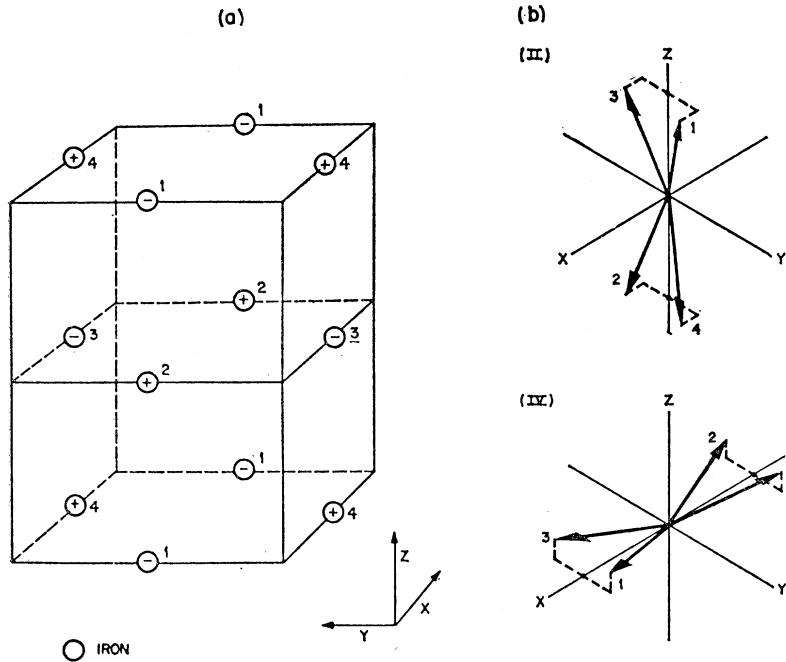[32] D. Treves, J. Appl. Phys. **36**, 1033 (1965).

(a)

(b)

(II)

FIG. 1. Magnetic structure of the ortho-
ferrites (taken from Herrmann, Ref. 33).
(a) Orthorhombic unit cell showing Fe^{3+}
sites and indexing them to the magnetic
sublattices. The numbers refer to the four-
sublattice model. The signs $\pm$ refer to a
two-sublattice model which neglects hidden
canting (see text). (b) Room-temperature
spin configurations. Numbers index the spins
to the magnetic sublattices shown in (a).

(IV)

○ IRON

the effective field of the Fe^{3+} ions, and for our purposes
their magnetization can be neglected (at room
temperature).

There are four possible spin configurations compatible
with the space group D_{2h}^{16}-$Pbnm$. These configurations
are described by the four distinct magnetic sublattices
shown in Fig. 1(a) after Herrmann.[33] The configurations
found in the orthoferrities at room temperature, II
and IV in the notation of Herrmann, are shown in
Fig. 1(b). $SmFeO_3$ has spin configuration II and the
other orthoferrites have configuration IV.

Figure 1(b) shows that there are two contributions
to the net spin cantings, one of which results in a net
magnetic moment and one that does not. For example,
in configuration IV the canting of the spins relative
to the xy plane results in a net magnetization, but the
symmetric canting of the spins relative to the xz plane
does not. The former are called overt cantings and the
latter are called hidden cantings. On the basis of
magnetization data the overt canting α is estimated to
be about 0.5° for all the orthoferrites. Unit-cell volumes
and Curie temperatures decrease gradually with dif-
ferent rare-earth ions going across the lanthanide
series in the Periodic Table from $LaFeO_3$ to $LuFeO_3$,
i.e., from low to high atomic number. While Y is not a
lanthanide element, $YFeO_3$ has a unit-cell volume and
Curie temperature nearly equal to those of $HoFeO_3$.
As R^{3+} varies from La^{3+} to Lu^{3+}, unit-cell volumes
decrease from 243.1 to 218.8 Å^3, and Curie tempera-
tures from 743 to 625°K.

---

[33] G. F. Herrmann, Phys. Rev. **133**, A1334 (1964).

B. Complex Polar Kerr Effect

1. Results

Polar Kerr effects were measured at room tempera-
ture between 1.8 and 5.5 eV for mirrorlike growth
surfaces of eleven single-crystal orthoferrities ($R=$ Sm,
Eu, Gd, Tb, Dy, Y, Ho, Er, Tm, Yb, Lu). These results
are presented in Fig. 2 and are available elsewhere
plotted on expanded scales.[35] The data are displayed
as double rotations and ellipticities, e.g., $\varphi = \varphi(\mathbf{M})$
$-\varphi(-\mathbf{M}) = 2\varphi(\mathbf{M})$, and are believed to be character-
istic of bulk, single-crystal materials (see Secs. III B 2
and IV A). The samples were magnetically saturated
along [001], i.e., normal to the measurement surface,
except for $SmFeO_3$, which was saturated along [100],
i.e., about 45° to the (110) measurement surface for
$SmFeO_3$.

Polar Kerr rotations were measured for all samples
and, as can be seen from Fig. 2, the results vary only
slightly with different rare earths. Polar Kerr elliptici-
ties, necessary for determination of the off-diagonal
elements, were measured for Sm, Eu, Tb, Dy, Y, Tm,
and Lu orthoferrites. We shall see that these appear to
be a sufficient number of samples to permit interpreta-
tion of all major trends and anomalies in the tensor
elements.

The error bars shown for the $EuFeO_3$ measurements
in Fig. 2 are representative of all the spectra. The low-
energy tails of the polar Kerr rotations for Eu, Er,
Yb, and Lu orthoferrites are plotted on an expanded
scale in Fig. 3. These plots demonstrate the high sensi-
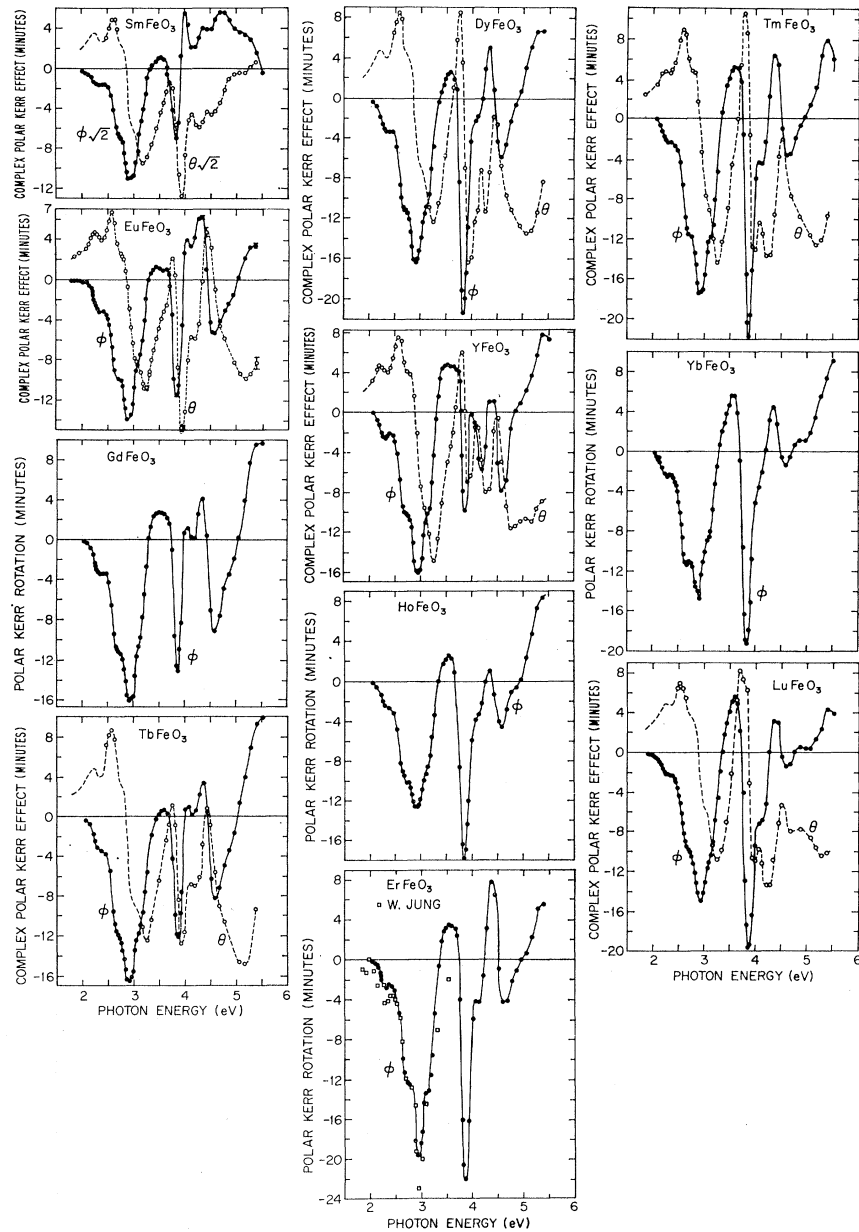tivity of the Kerr spectrometer designed and con-

FIG. 2. Composite of polar Kerr effects for all investigated orthoferrites. The Kerr data in this and subsequent figures are displayed as double rotations and ellipticities. For additional details, see text.

structed for this investigation.[3] Note the resolved local maxima for the rotations near 2.3 eV, which tend to shift towards lower energies in going from $EuFeO_3$ to $LuFeO_3$.

Prior to the current investigation, the most extensive magneto-optical measurements on the orthoferrites were the results of Jung[15] for a [001] growth surface of $ErFeO_3$ in the visible region. Representative points from his data are plotted for comparison with the present measurements in Fig. 2. The major dependences are the same, and the two sets of data are in reasonable agreement. The differences which do exist can be attributed to variations from sample to sample and to

scattering and possible calibration errors in Jung's apparatus.

The significant difference between the two sets of rotation measurements for $ErFeO_3$ shown in Fig. 2 is the new information in the ultraviolet contributed by the current investigation. The prominent peak at 3.87 eV, beyond the range of Jung's measurements, and the shoulder at 3.15 eV, unresolved in Jung's data, are of particular interest. These, together with the strong visible peak at 2.92 eV, play prominent roles in the microscopic theory of Sec. V.

Examination of the spectra of Fig. 2 shows that except for the anomalous behavior of $SmFeO_3$ above
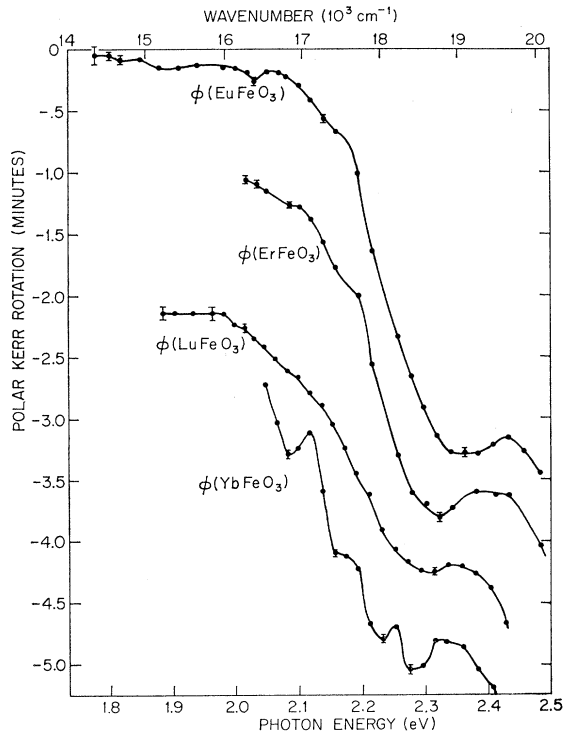
FIG. 3. Low-energy tails of polar Kerr rotations for Eu, Er, Yb, and Lu orthoferrites. For clarity, the rotation curves for Er, Lu, and Yb orthoferrities have been offset -1.0, -2.0, and -2.5 min, respectively.

4.35 eV and some low-energy details in Fig. 3, the spectral features of the materials investigated can be related on a one-to-one basis in intersample comparisons. There are variations of magnitude and shape, but, with the exceptions noted, all features can be traced across the orthoferrite series from $SmFeO_3$ to $LuFeO_3$. While the rare earths influence the spectra, these common features are present independently of the rare earth. It is therefore apparent that the transitions responsible for these spectral features are associated with the Fe^{3+}-O^{2-} sublattices.

We see from Sec. II that the physical properties giving rise to the observed magneto-optical spectra can be described by the elements ϵ_0 and ϵ_1 of the dielectric tensor $\boldsymbol{\varepsilon}$. Only ϵ_1 is linearly dependent on magnetization, and it is the appropriate physical property to be calculated from a microscopic model. The development of a microscopic model is therefore facilitated by determination of ϵ_1 from the experimental spectra. Knowledge of the diagonal element ϵ_0, will enable us to obtain ϵ_1 by application of Eq. (6): $\Phi = -i\epsilon_1/\epsilon_0^{1/2}(\epsilon_0-1)$. The diagonal and off-diagonal elements ϵ_0 and ϵ_1 are presented, and the methods by which they were obtained are described, in Secs. III C and III D. The remainder of the present section discusses the preparation and magnetic hysteresis of the samples used in the polar Kerr measurements.

2. Sample Preparation and Magnetic Hysteresis

The samples used in this investigation, including the ferrimagnetic materials discussed in Sec. IV, were grown by the flux method. All but the orthoferrities of the five lightest lanthanide elements were available with suitable growth surfaces. The orthoferrities of La, Ce, Pr, and Nd grow only with difficulty and with relatively high concentrations of Pb impurities; Pm is radioactive.

The growth surfaces were prepared for measurement by cleansing with a low-residue organic solvent. Care was taken to swab dry the surfaces before evaporation left a residue.

The orthoferrities are slightly soluble in hot concentrated nitric acid. In order to check on possible spurious surface effects, a sample of $TmFeO_3$ was etched by boiling for 15 min in concentrated nitric acid, allowed to cool, and then rinsed in glass-distilled water. The polar Kerr rotation was measured from 2.88 to 5.39 eV before and after etching. Absolutely no change was observed in the measured spectra. Furthermore, these spectra were identical to those of two additional unetched $TmFeO_3$ samples. These comparisons and the self-consistency of the measured spectra indicate that the measurements were not influenced by spurious surface effects. The properties measured are deemed to be characteristic of bulk, single-crystal materials.

While the direction of the weak ferromagnetic moment in the orthoferrites at room temperature cannot be reoriented with low external fields, it can be reversed relatively easily. All samples displayed rectangular hysteresis loops with sharp 90° corners as monitored by the polar Kerr effect. Fields required for magnetization reversal and saturation varied from about 50 to over 2000 Oe. Minor loops were accessible in a few samples and most prominent in $LuFeO_3$. The minor loops in $LuFeO_3$ resulted from simultaneous measurement of macroscopically separate regions of high and low coercivity. These coercivities were about 2500 and 750 Oe, respectively. Investigation showed the Kerr spectra to be independent of coercivity.

C. Dielectric Tensor: Diagonal Elements

1. Results

The complex diagonal elements $\epsilon_0 = \epsilon_0' + i\epsilon_0''$ and the complex index of refraction $n = n' + in''$ obtained from Kramers-Kronig analysis of the normal reflectivity data for $EuFeO_3$, presented in Fig. 4, are displayed in Fig. 5. While the principal reflectivity peaks at 3.0 and 3.85 eV are in close coincidence with the principal peaks in the Kerr rotation data of Fig. 2, the magneto-optical spectra show more structure.

The Kramers-Kronig analysis required extrapolation of the reflectivity data to zero and to infinite photon energies. We chose our extrapolation to provide a best fit to the results of Jung[15] for ϵ_0. Jung directly
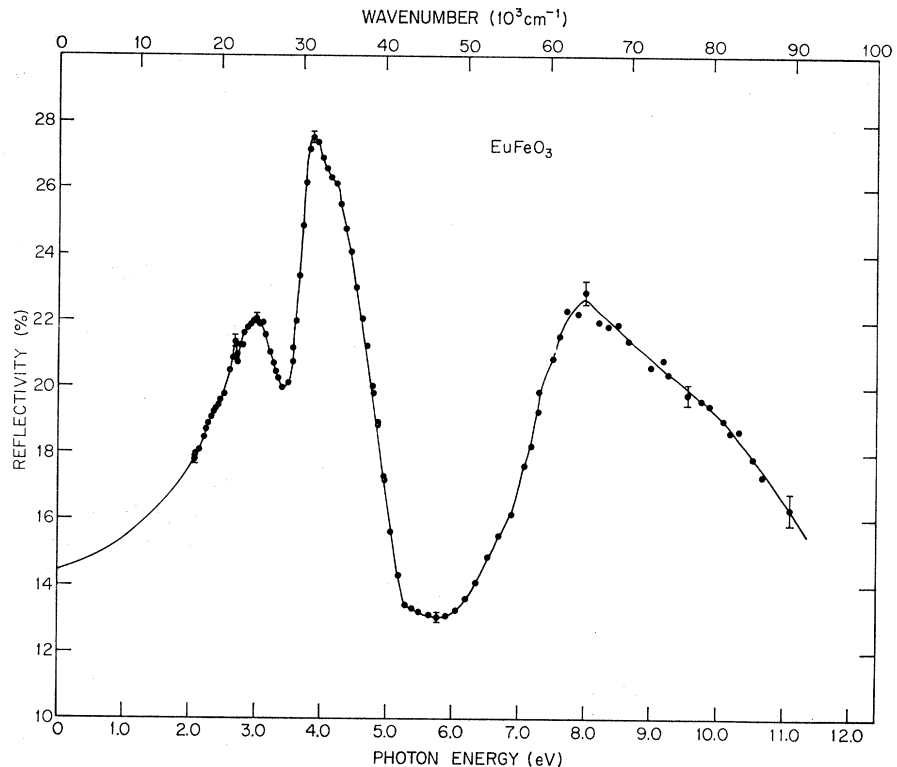
FIG. 4. Normal reflectivity of Eu orthoferrite (001) face. The reflectivity curve has been extrapolated to 0 eV for use in the Kramers-Kronig analysis. For further details, see text.

measured the diagonal tensor elements for $ErFeO_3$ in the visible region using an ellipsometer. Representative points from his data are plotted for comparison in Fig. 5(a). The agreement between the two sets of results is very good, especially considering the different methods by which they were obtained. Note that Jung's data are for $ErFeO_3$, while ours are for $EuFeO_3$, demonstrating that ϵ_0 and R vary vary little for orthoferrites with different rare-earth ions. These results for ϵ_0 will be used to obtain ϵ_1 in Sec. III D.

2. Kramers-Kronig Analysis

The diagonal elements were computed from the normal reflectivity data using a Kramers-Kronig program supplied by Grant of IBM, San Jose, Calif. For a general discussion of Kramers-Kronig methods see Sec. II D. The measured reflectivities were extrapolated at the high-energy end to infinite energy using the relation

$$R = R_m (E_m/E)^P, \qquad (20)$$

where E_m is the highest energy E for which the reflectivity R was measured. The extrapolation parameter P, about 3 for the spectrum of Fig. 4, was adjusted by the program so that the results agreed with a known value n_K of the complex index of refraction at one particular energy E_K. The best fit, shown in Fig. 5(a), was obtained with $n_K = 2.642 + i0.45$ for $E_K = 2.8$ eV. At the low-energy end, the reflectivities were extra-

polated by eye to zero energy. Infrared reflectivity data would have been preferred, but were not available.

These are common methods of extrapolation, known to provide good results. A general discussion of extrapolation procedures, including the methods employed above, is given by Stern.[27] As a rule of thumb, reflectivity should be measured to energies at least 50% higher than the highest energy for which accurate tensor elements are required. This rule tested satisfactorily on Cardona and Harbeke's results for ZnS[34] and was adopted.

3. Normal Reflectivity

a. Absolute reflectivity. The absolute, normal reflectivity R for a (001) growth face of $EuFeO_3$ has been presented in Fig. 4. The samples used for the reflectivity measurements were the same as those used for the polar Kerr measurements. No external field was required for the reflectivity measurements because $|\epsilon_1| \ll |\epsilon_0|$. The small pleochroism given by $|\epsilon_2| \ll |\epsilon_0|$ is also negligible. Reproducibility of the absolute reflectivity measurements was about $\pm 0.05R$. Relative errors are given by the error bars in Fig. 4.

Less accurate measurements of the normal reflectivity spectrum of $LuFeO_3$ showed it to have the same general shape as the $EuFeO_3$ spectrum, demonstrating that the straight reflectivity spectra are not appreciably altered by the different rare-earth ions. Recall our similar

---

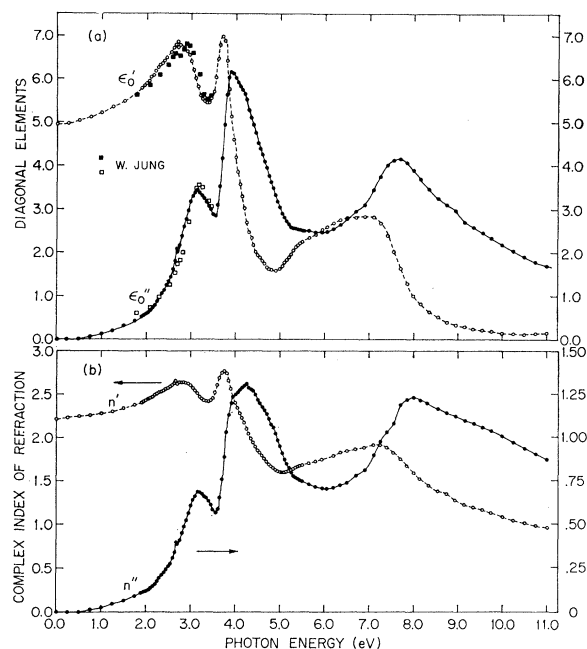[34] M. Cardona and G. Harbeke, Phys. Rev. **137**, A1467 (1965).

FIG. 5. Complex diagonal elements $\epsilon_0 = \epsilon_0' + i\epsilon_0''$ and complex index of refraction $n = n' + in''$ for Eu orthoferrite (001) face. The diagonal elements in (a) are compared with the results of Jung (Ref. 15) for $ErFeO_3$ in the visible (see text).

conclusion based on the comparison of ϵ_0 for $EuFeO_3$ and $ErFeO_3$ in Fig. 5(a). Grant observed similar behavior for iron garnets.[17]

If ϵ_1 for $EuFeO_3$ is computed using ϵ_0 derived from either R for $EuFeO_3$ or R for $LuFeO_3$, the results are similar. The dependence of the computed ϵ_1 on R, and on the extrapolation parameters for the Kramers-Kronig analysis, is discussed in detail in Sec. III D.

The absolute reflectivity data were measured at almost normal incidence (13.5°) with apparatus incorporating a McPherson model 225 1-m vacuum uv monochromator and a noncommercial dc-discharge H_2 capillary source. The photomultiplier alternately viewed the beam incident on and reflected from the sample. The ratio of these measurements provided the absolute reflectivity. 2-mm-slit openings resulted in a spectral half-width of 17 Å.

b. Relative reflectivity. To further substantiate the small variation of R with different rare earths, relative reflectivities were determined for eight orthoferrites ($R=$ Sm, Eu, Gd, Tb, Dy, Y, Tm, Lu) between 2.384 and 3.993 eV. The estimated error in these measurements is about $\pm 5\%$, of which about half is due to inaccuracies in sample alignment relative to the sharply focused spectrometer beam.

The relative reflectivities, computed for each sample at eight different energies and referred to the reflectivity of $LuFeO_3$ at the corresponding energies, are given in Table I. The observed variations in reflectivity are for the most part within the limits of experimental error. The relative reflectivities range from 0.92 to 1.07, and

84% of them fall within 6% of 1.00. These small variations have no major effect on the computed values for the off-diagonal elements. Therefore the absolute reflectivity data for $EuFeO_3$ will be used to compute ϵ_1 for all the orthoferrites.

The relative reflectivities were measured with apparatus incorporating a Perkin Elmer model 83 Universal Prism Monochromator and a quartz iodine-cycle tungsten lamp. Relative reflectivities were determined by alternately substituting samples and taking the ratio of the reflected intensities. The spectral half-width ranged from 6 Å at 3.99 eV to 30 Å at 2.88 eV.

D. Dielectric Tensor: Off-Diagonal Elements

1. Results

The off-diagonal elements ϵ_1, were determined for seven orthoferrites ($R=$ Sm, Eu, Tb, Dy, Y, Tm, and Lu) and are displayed in Fig. 6. The results are available elsewhere plotted on expanded scales.[35]

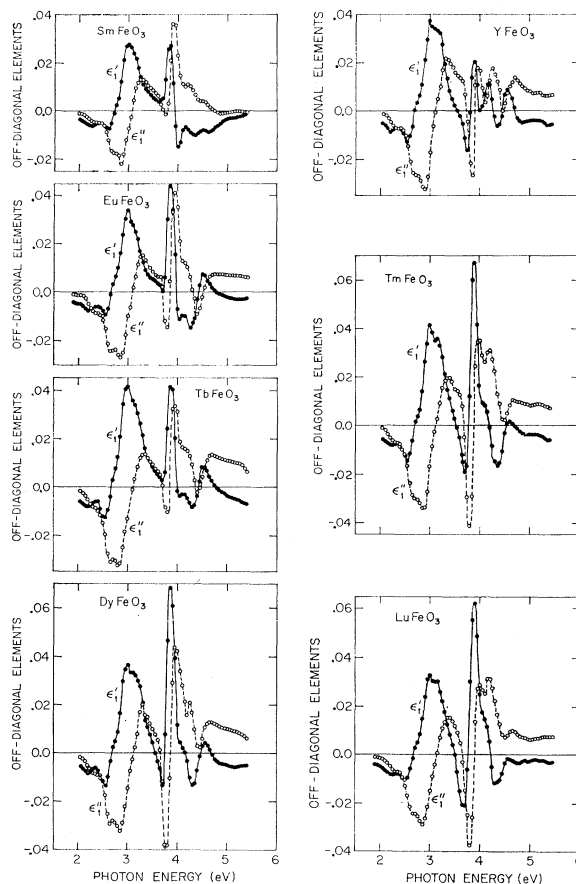FIG. 6. Composite of off-diagonal elements ϵ_1 for all investigated orthoferrites.

[35] F. J. Kahn, Ph.D. thesis, Harvard University, 1968 (unpublished).

TABLE I. Orthoferrite relative reflectivities (referred to $LuFeO_3$).

Energy (eV) \ R^{3+}	Sm	Eu	Gd	Tb	Dy	Y	Tm	Lu
3.993	1.069	1.037	1.044	0.982	0.979	1.008	0.961	1.0
3.821	1.053	1.055	1.074	0.963	0.978	1.007	0.983	1.0
3.636	1.022	1.030	0.994	0.942	1.009	0.949	0.971	1.0
3.459	0.922	0.997	0.953	0.938	1.037	0.929	0.963	1.0
3.271	0.961	0.976	0.936	0.948	0.990	0.937	0.972	1.0
3.061	0.948	0.973	0.948	0.939	0.949	0.952	0.962	1.0
2.818	0.970	0.989	0.951	0.972	0.973	0.946	0.991	1.0
2.384	0.986	1.003	0.947	0.994	0.986	0.919	0.983	1.0
Average	1.000	1.007	0.981	0.960	0.988	0.956	0.973	1.0

Off-diagonal elements for $ErFeO_3$ in the visible region were derived by Jung,[15] who employed a method valid only for weakly absorbing media. Not having measured θ directly, Jung determined θ by assuming it and φ to be conjugate variables satisfying Kramers-Kronig relations of standard form.[19] He then calculated ϵ_1 using his ellipsometric results for ϵ_0. We have indicated (Sec. II D) that these relations do not apply to $\Phi = \varphi + i\theta$ when ϵ_0 is strongly energy-dependent, i.e., in the region of strong absorption. Therefore Jung's results are only approximately valid for the orthoferrites in the visible region, where ϵ_0 is already starting to show a strong energy dependence. His method would be invalid in the uv. Our results show qualitative agreement with those of Jung in the visible.

In Sec. II D it was pointed out that ϵ_1 satisfies the Kramers-Kronig relations and that these relations imply correlations in frequency of the extrema of ϵ_1 given by Eq. (19). The results for ϵ_1 satisfy Eq. (19), thereby confirming the self-consistency of our measurements, computations, and sign conventions.

The off-diagonal elements, with exception of those for $SmFeO_3$, whose spectrum is anomalous above 4.35 eV, vary relatively little with different rare earths. There are some variations in shape and magnitude, but, with the exception noted, all features can be traced through the orthoferrite series on a one-to-one basis. These common spectral features are therefore associated with the Fe^{3+}-O^{2-} sublattices. A microscopic theory attributing these spectra to transitions between molecular orbitals of octahedral $Fe^{3+} \cdot 6O^{2-}$ complexes is presented in Sec. V.

2. Origin of Variations in ϵ_1

The off-diagonal elements ϵ_1 of Fig. 6 are computed elements whose values were determined using ϵ_0 for $EuFeO_3$. Thus the variations in ϵ_1 with different rare-earth ions may arise either from actual differences in ϵ_1 or from failure to account for differences in ϵ_0 when we computed ϵ_1 for these materials. In the discussion which follows we denote the computed values by ϵ_{1C}.

Concentrating on ϵ_{1C}', we observe that among the largest variations are those in the relative magnitudes

of the ϵ_{1C}' maxima at 3.00 and 3.85 eV and in the line shape of ϵ_{1C}' between 3.7 and 4.3 eV. The resemblance in line shapes between ϵ_{1C}'' (ϵ_{1C}') for $EuFeO_3$ and ϵ_{1C}' ($-\epsilon_{1C}''$) for $LuFeO_3$ in the 3.7–4.3-eV region is particularly striking. We will show that the close agreement in *shape* between the measured reflectivities, and therefore between the diagonal elements, indicates that the line-shape differences in ϵ_{1C} originate in the off-diagonal elements ϵ_1 themselves. In contrast, we will also show that relatively small magnitude variations in R, and hence in ϵ_0, can result in considerably larger variations in ϵ_{1C}, thereby accounting for the *magnitude* variations in the latter.

One parameter whose value does not matter very much is R_0, the reflectivity at zero energy, to which R has been extrapolated. Our results are relatively insensitive to R_0 because zero energy lies well outside the energy range of interest for ϵ_1. The Kramers-Kronig relations show that $\epsilon_0(E)$ is most sensitive to $R(E')$ for small $|E-E'|$. Thus the effect of R_0 is small in comparison to the effects of the directly measured reflectivities $R_m(E')$ and the known value $n_K(E_K)$ which lie within the energy range of interest.

Suppose that $R(E) = fR_m(E)$, where the constant factor f accounts for possible errors in the measured absolute reflectivities R_m. The values for ϵ_{1C}' for $EuFeO_3$ are given in Fig. 7(a), where the diagonal elements used to compute ϵ_{1C}' have been obtained by Kramers-Kronig analysis of R for $f = 0.9$, 1.0, 1.1. The $EuFeO_3$ data of Fig. 4 were used for R_m. In computing the results of Fig. 7(a) we have taken $n_K'' = 0.45$ at $E_K = 2.8$ eV for all three cases. The effect of $f = 1.1$
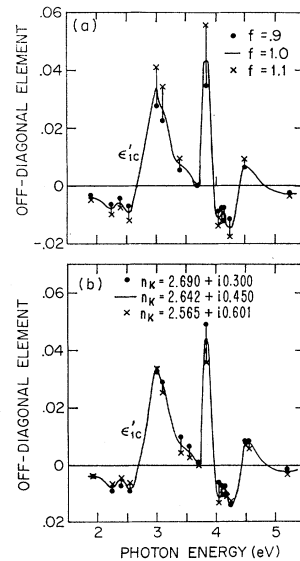
FIG. 7. Variations in ϵ_{1c} due to variations in input to Kramers-Kronig analysis for ϵ_0 (a) Dependence of ϵ_{1c}' on reflectivity scale factor f, where $R = fR_m$ and R_m is the measured reflectivity. (b) Dependence of ϵ_{1c}' on known refractive index n_K at 2.8 eV. Note that n_K determines the extrapolation parameter P. For additional details, see text.

(0.9) is to increase (decrease) the magnitude of ϵ_{1C}' almost uniformly at all energies. No line-shape distortion results, but relatively small changes in R give rise to relatively large magnitude changes in ϵ_{1C}'. For example, if the actual reflectivity R is 10% larger than the value R_m used in computing ϵ_{1C}', i.e., $f=1.1$, then at 3.85 eV, ϵ_1' will be 27% larger than ϵ_{1C}'.

Even if there are no measurement errors, an energy-dependent f is expected to be applicable to our results because reflectivities measured for one orthoferrite, $EuFeO_3$, have been used to determine ϵ_{1C} for all the orthoferrites. While the variation of $\epsilon_{1C}(E)$ due to $f(E)$ would be somewhat more complicated than in the simpler case of constant f just discussed, the final results should be qualitatively similar. Small variations in the relative reflectivities of the various orthoferrites will give rise to several times larger variations in the magnitude of ϵ_{1C}. For example, at 3.82 eV the measured relative reflectivity of $EuFeO_3$ to that of $LuFeO_3$ is 1.055; therefore ϵ_{1C}' should be roughly 5.5 (2.7)=15% higher for $LuFeO_3$ than for $EuFeO_3$ if we assume ϵ_1' to be the same for both materials. It is in fact 14% higher.

Thus, while the magnitude variations in ϵ_{1C}' can be attributed to actual variations in ϵ_1', they may also originate in the diagonal elements ϵ_0. On the other hand, we now show that line-shape variations of the type observed in ϵ_{1C} between 3.7 and 4.3 eV should be attributed to differences in ϵ_1 and not in ϵ_0.

The only variable parameter whose effects have not been considered is n_K. The off-diagonal elements ϵ_{1C}' for $EuFeO_3$ are given in Fig. 7(b) for $n_K = 2.690 + i0.300$, $2.643 + i0.450$, and $2.565 + i0.601$ at $E_K = 2.8$ eV. R was taken from Fig. 4. The values for n_K were chosen so as not to change the reflectivity at E_K. The changes induced by varying n_K over a considerable range are seen to be of little consequence. Variation of n_K results in qualitative changes in the shape of ϵ_{1C}' between 4.0 and 4.25 eV of the type observed for different rare
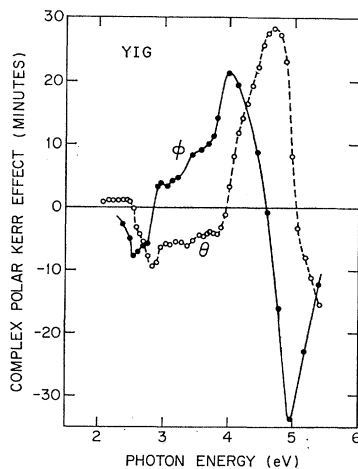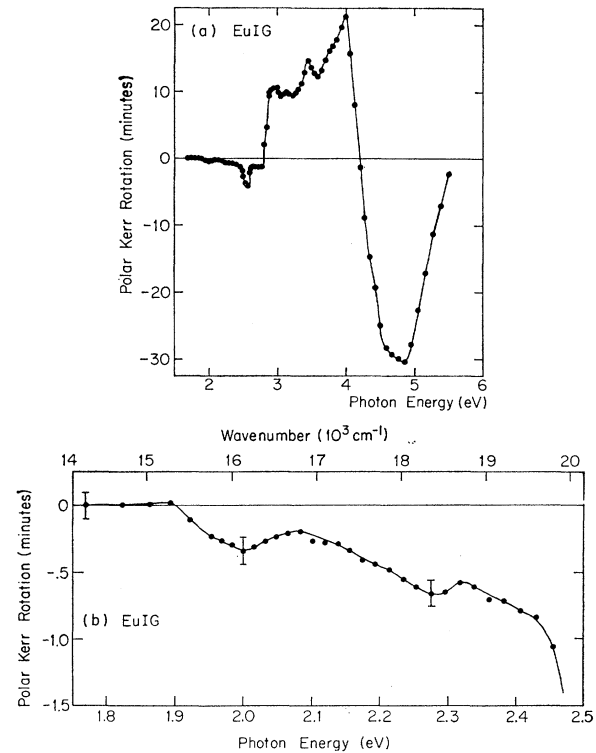

FIG. 9. Polar Kerr rotations φ for europium iron garnet (110) face.

earths. However, these changes due to n_K are much too small to explain the observed variations quantitatively. For example, note from Fig. 6 that $\epsilon_{1C}' \gg 0$ for $LuFeO_3$ at 4.05 eV while $\epsilon_{1C}' \ll 0$ for $EuFeO_3$ at the same energy. This large line-shape variation could not be accounted for by variations in n_K.

We conclude that while the variations in amplitude of ϵ_{1C} for different rare-earth orthoferrites can be attributed to changes in either ϵ_1 or ϵ_0, the line-shape variations in ϵ_{1C} are attributed to physical processes unique to ϵ_1, e.g., spin-orbit interaction. However, all these variations are small and of relatively minor consequence for our current purposes—the development of a qualitative microscopic model. Therefore ϵ_{1C} for $EuFeO_3$ will be considered for purposes of the microscopic analysis in Sec. V as being representative of ϵ_1 for all the orthoferrites. $EuFeO_3$ is the best choice because the most accurate absolute reflectivity measurements were made for this material.

IV. FERRIMAGNETIC FERRIC OXIDE COMPOUNDS

A. Rare-Earth Iron Garnets

1. Pure Systems

The optical and magneto-optical properties of the ferrimagnetic ferric oxide compounds are considerably more complicated than those of the orthoferrites
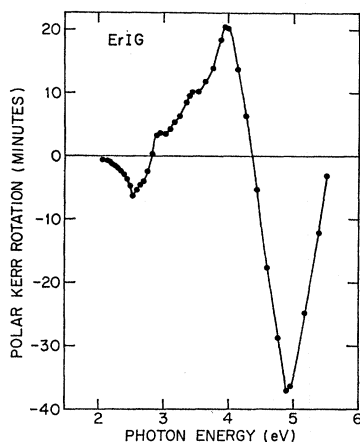

FIG. 8. Complex polar Kerr effect $\Phi = \varphi + i\theta$ for yttrium iron garnet (110) face.

Fig. 10. Polar Kerr rotation φ for erbium iron garnet (110) face.

because the ferrimagnetic compounds contain additional types to iron sites. In particular, the ferrimagnetic compounds contain both tetrahedral (Fe^{3+}_{tet}) and octahedral (Fe^{3+}_{oct}) iron sites. Within this class of materials, the rare-earth iron garnets[7,36,37] were chosen for the most detailed studies because they are one of the simpler ferrimagnetic systems from the perspective of this investigation, can be modified to distinguish between the tetrahedral and octahedral contributions to the magneto-optical spectra, and can be grown with a high degree of perfection.

The ideal rare-earth iron garnets, formula $\{R^{3+}_3\}$ $[Fe^{3+}_2](Fe^{3+}_3)$ O^{2-}_{12} and space group $O_h^{10}\text{-}Ia3d$, have a cubic crystal structure with eight formula groups per unit cell. There are three Fe^{3+}_{tet}, two Fe^{3+}_{oct}, and three R^{3+} ions per formula unit. Both Fe^{3+} and R^{3+} have only O^{2-} ions for nearest neighbors.

The strongest magnetic interaction is an antiferromagnetic one between the Fe^{3+}_{oct} and Fe^{3+}_{tet} ions. The next strongest interaction, also antiferromagnetic, is between the Fe^{3+}_{tet} and R^{3+} ions. The net magnetization is that of the Fe^{3+}_{tet} sublattice minus the sum of the magnetizations of the Fe^{3+}_{oct} and R^{3+} sublattices for rare earths in the second half of the lanthanide series. Rare-earth ions in the first half of the lanthanide series have their magnetizations aligned parallel to Fe^{3+}_{tet} because they have $J = L - S$ rather than $J = L + S$. Néel temperatures are above 548°K, and at room temperature the Fe^{3+}_{tet} magnetizations dominate the magnetizations of both Fe^{3+}_{oct} and R^{3+}. The Fe^{3+} ions absorb much more strongly than the R^{3+} ions in the energy range of interest. Thus the room-temperature optical as well as magnetic properties are determined primarily by the Fe^{3+} ions.

The Fe^{3+}_{oct} and Fe^{3+}_{tet} ions have point symmetries $\bar{3}$ and $\bar{4}$, respectively. Although the Fe-O distances within the oxygen polyhedra are constant, the poly-

hedra are distorted in shape.[37,38] As in the orthoferrites, the garnet unit cell dilates with increasing rare-earth ion radii.[7,39]

The rare-earth iorn garnets have [111] easy, [100] hard, and [110] intermediate easy directions.[40] Because the largest growth faces tend to be {110} and {211} planes, the {110} faces are the most suitable for polar Kerr measurements.

The complex polar Kerr effect for a {110} face of yttrium iron garnet (YIG) is given in Fig. 8. The YIG results were measured at about 95% of saturation in the direction normal to the surface. The polar Kerr rotations at saturation for {110} faces of EuIG and ErIG are displayed in Figs. 9 and 10. The one-to-one correspondence between the rotation peaks in the YIG, EuIG, and ErIG samples shows that the linear magneto-optical effects in the rare-earth iron garnets are associated with the Fe-O sublattices. As for the orthoferrites, the Kerr data are displayed as double rotations and ellipticities, e.g., $\varphi = \varphi(\mathbf{M}) - \varphi(-\mathbf{M}) = 2\varphi(\mathbf{M})$.

The sign differences between the major rotation peaks near 2.5, 4.0, and 5.0 eV are important and will be discussed later. The magnitude of these rotations is also very significant. The net contribution of the Fe^{3+} sublattices to the total magnetization of the ferrimagnetic iron garnets,[41] i.e., the magnetization exclusive of the contributions of the rare-earth ions, is 17 times larger than that of the weakly ferromagnetic orthoferrites.[10] Since the rotations for both crystal types originate with similarly coordinated Fe^{3+} ions, we might expect the polar Kerr rotation to be over an order of magnitude larger for the garnets than for the orthoferrites. However, the maximum peak rotation
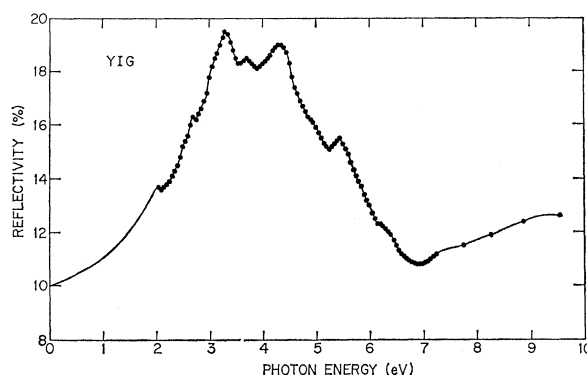
Fig. 11. Normal reflectivity of yttrium iron garnet. The reflectivities shown between 2.05 and 7.25 eV are those of Grant (Ref. 17). The points are not the experimental ones, but indicate the grid used for the Kramers-Kronig analysis. The curve between 0 and 2.05 eV is the low-energy extrapolation for the Kramers-Kronig analysis.

[36] B. Lax and K. Button, *Microwave Ferrites and Ferrimagnetics* (McGraw-Hill Book Co., New York, 1962), Chap. 3.

[37] S. C. Abrahams and S. Geller, Acta Cryst. **11**, 437 (1958).

[38] F. Euler and J. A. Bruce, Acta Cryst. **19**, 971 (1965).

[39] L. Néel, R. Pauthenet, and B. Dreyfus, Progr. Low Temp. Phys. **4**, 344 (1964).

[40] G. P. Rodrigue, Ph.D. thesis, Harvard University, 1958 (unpublished).

[41] *Handbook of Microwave Ferrite Materials*, edited by W. H. von Anloch (Academic Press Inc., New York, 1965), p. 78.
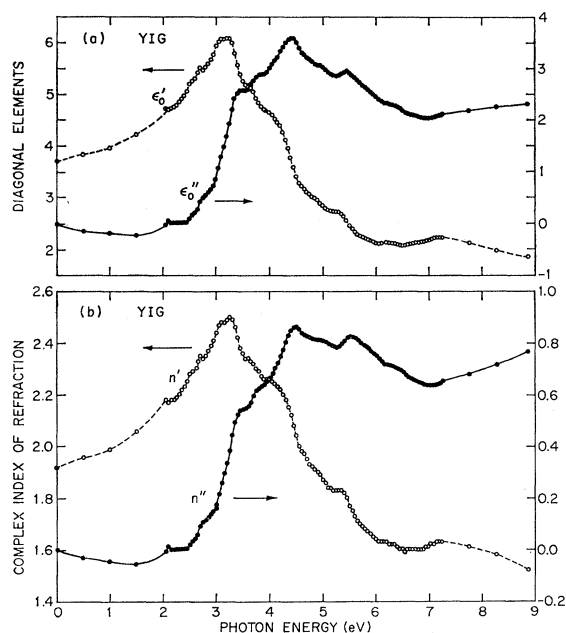
FIG. 12. Complex diagonal elements $\epsilon_0 = \epsilon_0' + i\epsilon_0''$ and complex index of refraction $n = n' + in''$ for yttrium iron garnet.

(double rotation) for the investigated garnets, -37 min at 4.95 eV for ErIG, is only 1.7 times the maximum peak rotation for the orthoferrites, -22 min at 3.87 eV for $ErFeO_3$ (Fig. 2). There is an order of magnitude discrepancy in the expected and observed rotations. We will show in Sec. V that this apparent anomaly can be explained by anisotropic orbital quenching. As a result of the different spin configurations of these materials, anisotropic quenching can significantly enhance the magneto-optical effects in the weakly ferromagnetic orthoferrites while causing relatively little change in the magnitude of magneto-optical effects in the ferrimagnetic ferric oxide compounds.

The absolute reflectivity R for YIG at room temperature is given in Fig. 11. The reflectivities shown between 2.05 and 7.25 eV are those of Grant,[17] who independently measured the reflectivity of YIG in this range. Our results were in semiquantitative agreement with his but were affected by source instabilities which appeared after the $EuFeO_3$ spectrum of Fig. 4 was measured.

The diagonal elements ϵ_0 and complex refractive index n obtained from Kramers-Kronig analysis of the YIG reflectivities are displayed in Fig. 12. The reflectivity curve between 0 and 2.05 eV in Fig. 11 shows the low-energy extrapolation used for the Kramers-Kronig analysis (see Sec. III C). The known value, for determination of P, was taken to be $n_K = 2.19 + i0.005$ at 2.25 eV. The value for n_K'' was obtained from the transmission measurements of absorption coefficient by Wood and Remeika.[16] The values for n_K'' and $R(E_K)$ then determined n_K'. Choice of too small an R_0, the extra-

polated zero-energy reflectivity, resulted in physically unrealistic negative values for ϵ_0'' between 0 and 2.05 eV in Fig. 12(a). R_0 was not adjusted further because of its small effect on ϵ_0 and ϵ_1 in the energy range of interest (Sec. III D).

The off-diagonal elements ϵ_1 for YIG, obtained from Φ of Fig. 8, ϵ_0 of Fig. 12(a), and Eq. (6), are plotted in Fig. 13. They will be utilized in the microscopic discussion of Sec. V as well as in the following calculation.

MacDonald et al.[18] have measured φ_T, the Faraday rotation in transmission, for a thin polycrystalline GdIG film. We can calculate φ_T for a single-crystal film of YIG using ϵ_1 from Fig. 13, ϵ_0 from Fig. 12(a), and Eq. (7). The result of this calculation, plotted in terms of degrees of rotation per micron of optical path length, are compared in Fig. 14 with results of MacDonald et al. which we have similarly normalized. The agreement is excellent in view of the difference in the materials and in the methods by which the two sets of results were obtained. Note that the zero crossings of φ_T near 3.3 eV are particularly sensitive to the diagonal tensor elements of the materials being measured and in the case of our results to the value for ϵ_0 used in calculating φ_T. The excellent agreement serves as another confirmation of the accuracy and self-consistency of our approach to obtaining the tensor elements ϵ_1.

2. Substituted Systems

Substituted garnet systems can also be grown.[7] In particular, diamagnetic Ga^{3+} substitutes preferentially for Fe^{3+}_{tet}, thereby permitting discrimination between the spectral contributions of Fe^{3+}_{tet} and Fe^{3+}_{oct}. The preference of Ga^{3+} for the tetrahedral Fe^{3+} sites de-
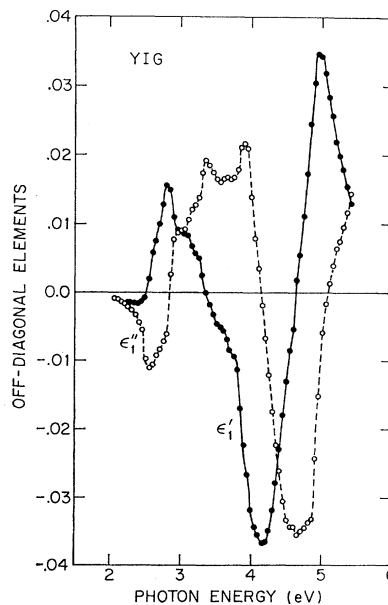

FIG. 13. Off-diagonal elements $\epsilon_1 = \epsilon_1' + i\epsilon_1''$ for yttrium iron garnet.
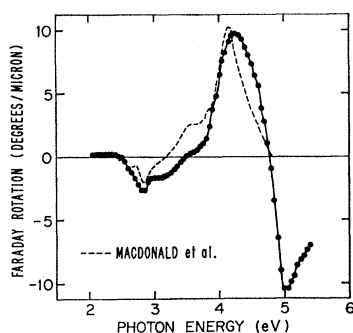
FIG. 14. Faraday rotation in transmission for yttrium iron garnet. The Faraday rotation φ_T, computed from the results of the current investigation for single-crystal materials, is compared with the measurements of MacDonald et al. (Ref. 18) for a thin polycrystalline film.

creases with increasing Ga^{3+} concentration.[42] For the system $Eu_3 Fe_{5-x} Ga_x O_{12}$, Marezio et al.[43] have shown that 91% of the Ga ions are found at tetrahedral sites for $x = 3.06$. We were limited to low Ga dopings because the Néel temperature passes through room temperature near $x = 2$. Therefore the Ga preference for the tetrahedral sites was well over 0.91 for all samples measured.

Polar Kerr rotations at saturation for (110) faces of the system $Eu_3 Fe_{5-x} Ga_x O_{12}$ ($0 \leq x \leq 1.9$) are presented in Fig. 15. The values given for x are the concentrations of Ga actually in the samples as determined by x-ray fluoresence analysis and by x-ray measurement of the lattice constants. The actual Ga concentrations, the Ga concentrations in the melts from which the crystals were grown, and the lattice constants for the samples measured are, respectively, (0.8, 1.0, 12.487 Å), (1.2, 1.5, 12.480 Å), (1.5, 1.7, 12.475 Å), and (1.9, 2.0, 12.469 Å).

As the Ga concentration is increased, the garnet magnetization goes through zero, i.e., a room-temperature magnetic compensation point. Passage through such a compensation point is marked by a change in sign of the polar Kerr rotation, since φ is tied not to the net magnetization but to the magnetization of the individual sublattices. If the small percentage of Ga ions substituting at octahedral sites, the magnetization of the Eu sublattice, and thermal disordering of the spins are neglected, the magnetic compensation point will occur when there are equal numbers of Fe^{3+}_{oct} and Fe^{3+}_{tet} ions, i.e., when $x = 1$. The measured polar Kerr rotation reverses sign between $x = 0.8$ and $x = 1.2$, thereby demonstrating not only the magnetic compensation point but also the validity of using garnet growth surfaces to observe bulk effects (see Sec. III B 2). It also proves that the observed spectra are not artifacts of the experimental system, a major source of concern in all magneto-optical measurements.

Since the Néel temperature approaches room temperature with increasing Ga concentration, the sublattice magnetizations and the measured polar Kerr rotation decrease with increasing x. Because the Ga ions substitute preferentially for Fe^{3+}_{tet} ions, the rotations associated with tetrahedral sites decrease much more rapidly than those associated with octahedral sites. We conclude from Fig. 15 that all the major rotations in the rare-earth iron garnets are associated with Fe^{3+}_{tet} ions, with the exception of the rotation peak at about 4 eV, which decreases relatively slowly and is therefore associated with Fe^{3+}_{oct}. These identifications will be helpful in analyzing the polar Kerr rotation spectra for the other ferrimagnetic ferric oxide compounds.

B. Spinel Ferrites

The spinel ferrites,[36,44–46] formula $(M^{2+}_x Fe^{3+}_{1-x})$ $[M^{2+}_{1-x} Fe^{3+}_{1+x}] O_4$ and space group O_h^7, have eight formula groups per cubic unit cell.[6] M is typically a metal ion such as one of the transition-metal ions or Mg. The parentheses and square brackets denote, respectively, ion sites tetrahedrally and octahedrally coordinated with O^{2-} ions. For $x = 1$, all Fe^{3+} ions are in octahedral sites and the resulting crystal is a normal spinel. For $x = 0$, the Fe^{3+} ions are evenly distributed between octahedral and tetrahedral sites and the result is an inverse spinel.

The dominant magnetic interaction is antiferromagnetic between octahedral and tetrahedral magnetic ions. Only inverted or partially inverted spinels have spontaneous magnetizations. The net magnetization is the difference between the magnetizations of the octa-
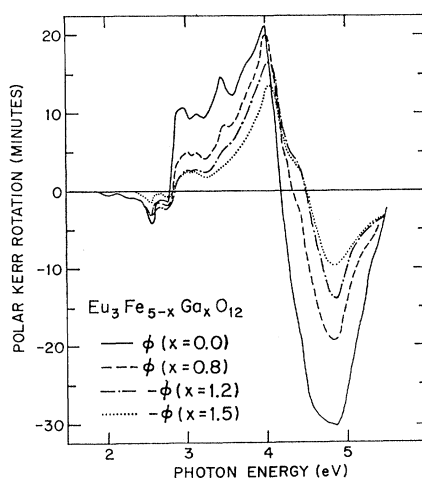
FIG. 15. Polar Kerr rotation φ for (110) faces of the Ga-substituted garnet crystals $Eu_3Fe_{5-x}Ga_xO_{12}$ ($0 \leq x \leq 1.5$). The Ga^{3+} ions substitute perferentially at the Fe^{3+}_{tet} sites. For $x = 1.9$ the maximum rotation observed was -1.3 min at about 4 eV.

[42] M. A. Gilleo and S. Geller, Phys. Rev. **110**, 73 (1958).
[43] M. Marezio, J. P. Remeika, and M. Zocchi, J. Chem. Phys. **48**, 1094 (1968).

[44] G. Blasse, Philips Res. Rept. Suppl. **3**, (1964).
[45] G. Blasse, Progr. Ceram. Sci. **4**, 134 (1966).
[46] A. H. Morrish, *The Physical Principles of Magnetism* (John Wiley & Sons, Inc., New York, 1965), Chap. 9.
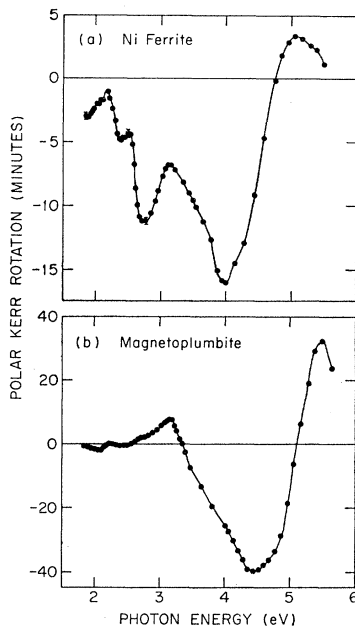
Fig. 16. Polar Kerr rotation φ for (111) face of nickel ferrite and (0001) face of magnetoplumbite.

hedral and tetrahedral sublattices. More complicated magnetic structures and site distributions occur and are discussed in the references.

The simple spinels have Néel temperature above 573°K, and except for Co ferrite, have [111] easy directions. The sum of the magnetizations of the M^{2+} and Fe^{3+} octahedral sublattices is greater than the sum of the magnetizations of the tetrahedral sublattices. Therefore the moments of Fe^{3+}_{oct} and Fe^{3+}_{tet} align, respectively, parallel and antiparallel to an external field. This is just the reverse of the Fe^{3+} alignment in the unsubstituted rare-earth iron garnets at room temperature.

The polar Kerr rotation for a (111) face of the inverse spinel (Fe) [NiFe] O_4 (Ni ferrite) at about 87% of saturation is given in Fig. 16(a). Analysis of this spectrum is more difficult than for the iron garnets because contributions from Ni^{3+}_{oct} ions as well as from Fe^{3+}_{tet} and Fe^{3+}_{oct} ions must be considered.

However, we can identify the major uv rotation peaks at 4 and 5.05 eV as being associated with the Fe^{3+}_{oct} and Fe^{3+}_{tet} sublattices, respectively. The supporting evidence for these assignments is as follows. These peaks have opposite signs and therefore must be associated with oppositely oriented magnetic sublattices if they are assumed to have similar microscopic origins. In addition, their energies coincide with the 4- and 5-eV principal rotation peaks for the garnets (Figs. 8–10) which were identified through the measurements on Ga-substituted EuIG (Fig. 15) as being associated with the Fe^{3+}_{oct} and Fe^{3+}_{tet} sublattices, respectively. Furthermore, the signs of the rotations in Ni ferrite are opposite to the signs of the rotations in the garnets, as would be

expected from the reversed alignments of the corresponding garnet and ferrite Fe^{3+} sublattices in an external field.

In addition to this identification of the uv rotation extrema, the gradual increase in rotation between 2.1 and 1.85 eV is tentatively attributed to the Ni^{2+} sublattice. The supporting evidence in this case is that significant rotations below 2.2 eV are not observed in any of the other ferric oxide compounds investigated. This identification is further supported by recent experimental results of Zanmarchi and Bongers,[47] who have measured the Faraday rotation of Ni, Mg, and Li spinel ferrites by transmission in the infrared between 0.155 and 1.24 eV.

C. Hexagonal Ferrites

The simplest hexagonal-structured ferric oxide compound[5,48] has the formula $PbO \cdot 6Fe_2O_3$ and the structure of the mineral magnetoplumbite by whose name it is commonly known. Ferrimagnetic magnetoplumbite has nine Fe^{+3}_{oct} ions, of which seven have spin up and two spin down; two Fe^{3+}_{tet} ions, both with spin down; and one hexahedrally coordinated Fe^{3+} ion, with spin up. Its Néel temperature is over 700°K and its easy axis is along [0001]. Magnetoplumbite grows with relatively large mirror-perfect (0001) growth surfaces, making it a particularly good material from the experimental point of view for polar Kerr measurements. However, the complicated magnetoplumbite crystal structure makes detailed analysis of its spectrum particularly difficult.

The polar Kerr rotation for a (0001) growth surface of magnetoplumbite at about 93% of saturation is given in Fig. 16(b). The peak double rotation of −40 min at 4.43 eV is the largest rotation we have observed in any of the ferric oxide compounds. The uv rotation peaks at 4.43 and 5.5 eV are attributed to Fe^{3+}_{oct} and Fe^{3+}_{tet}, respectively, for the reasons given in the similar assignments for Ni ferrite. These principal uv rotation peaks have been found in all the ferric oxide compounds studied. We show in the next section that they may be attributed to charge-transfer transitions in which an electron initially localized on a oxygen ion is excited into a molecular orbital localized on one of the ferric ions.

V. MICROSCOPIC THEORY

A. Dielectric Tensor

1. Introduction

The dielectric tensor is the mathematical concept by which microscopic theory and laboratory experiment are related. In the preceding sections we have computed tensor elements from experimental observ-

[47] G. Zanmarchi and P. F. Bongers, J. Appl. Phys. 40, 1230 (1969).

[48] J. S. Griffith, The Theory of Transition-Metal Ions (Cambridge University Press, Cambridge, 1961).

ables. In this section we compute the tensor elements from a microscopic model.

2. Electric-Dipole Transitions

The contributions of allowed magnetic-dipole transitions are orders of magnitude too small to account for the observed spectra.[9,48] The spectra must therefore be interpreted in terms of electric-dipole transitions which have considerably greater oscillator strengths.

For a material with N saturated spin systems per unit volume in orbital singlet ground states $|g\rangle$, the contributions of electric-dipole transitions to the diagonal tensor elements, Eq. (2), are given by[49]

$$\epsilon_0 = 1 + \sum_e \epsilon_{0e} = 1 + \sum_{e,\nu} \epsilon_{0e(\nu)}$$

$$= 1 + \frac{4\pi N e^2}{m} \sum_{e,\nu} f_{ge(\nu)}$$

$$\times \frac{\omega_{ge(\nu)}^2 - \omega^2 + \Gamma_{ge(\nu)}^2 - 2i\omega\Gamma_{ge(\nu)}}{(\omega_{ge(\nu)}^2 - \omega^2 + \Gamma_{ge(\nu)}^2)^2 + 4\omega^2\Gamma_{ge(\nu)}^2}, \quad (21)$$

where for narrow lines, i.e., for $\Gamma_{ge(\nu)}/\omega_{ge(\nu)} \ll 1$,

$$f_{ge(\nu)} = (2m\omega_{ge(\nu)}/\hbar)|\langle g|x|e(\nu)\rangle|^2 \quad (22)$$

is the oscillator strength of the transition $|g\rangle \rightarrow |e(\nu)\rangle$,[48] and $\Gamma_{ge(\nu)}$ is the half-width at half-maximum of this transition's contribution to $\epsilon_0''(w)$. For broad lines $f_{ge(\nu)}$ and $\Gamma_{ge(\nu)}$ are still measures of the oscillator strength and linewidth. The sum in Eq. (21) is taken over all excited states $|e(\nu)\rangle$, where ν indexes the orbital degeneracy. Equation (21) applied rigorously to materials for which $|\epsilon_0 - 1| \ll 1$. For materials with larger dielectric constants, corrections must be made for local-field effects. At optical frequencies, these corrections, although not large, should be made. In any event, they will probably not change the qualitative conclusions to be drawn in this section. Since all systems are initially in the ground state, the subscript g will be dropped from f, ω, and Γ in subsequent expressions.

To first order in $\Gamma_{e(\nu)}/\omega_{e(\nu)}$, $\epsilon_{0e(\nu)}''$ is a maximum for $\omega = \omega_{e(\nu)}$. We find from Eq. (21)

$$f_{e(\nu)} = (m/2\pi N e^2)\omega_{e(\nu)}\Gamma_{e(\nu)}\epsilon_{0e(\nu)}''_{\max}, \quad (23)$$

a useful relation for calculating oscillator strengths from experimental spectra.

The contributions of electric-dipole transitions to the off-diagonal tensor elements, Eq. (2), are given by

$$\epsilon_1 = \sum_e \epsilon_{1e} = \sum_{e,\nu} \epsilon_{1e(\nu)}$$

$$= \frac{2\pi N e^2}{m} \sum_{e,\nu} \frac{f_{-e(\nu)} - f_{+e(\nu)}}{\omega^2 - \omega_{e(\nu)}^2 - \Gamma_e^2 - 2i\omega\Gamma_{e(\nu)}} \frac{\omega - i\Gamma_{e(\nu)}}{\omega_{e(\nu)}}, \quad (24)$$

[49] N. Bloembergen, *Nonlinear Optics* (W. A. Benjamin, Inc., New York, 1965), p. 27.

where

$$f_{\pm e(\nu)} = (m\omega_{e(\nu)}/\hbar)|\langle g|x \pm iy|e(\nu)\rangle|^2 \quad (25)$$

are oscillator strengths for circularly polarized transitions, and all other quantities are as previously defined. Shen[50] has derived an equivalent expression for ϵ_1. Linear magneto-optical effects occur only when $\epsilon_1(\mathbf{M})$ is nonzero and an odd function of the magnetization (or an externally applied magnetic field). For a system with inequivalent magnetic sublattices, $\mathbf{M}$ need not be macroscopically observable for a nonzero. linear magneto-optical effect to occur. For example, recalling for the garnet system $Eu_3\,Fe_{5-x}\,Ga_x\,O_{12}$ that the microscopic $\mathbf{M}$ equals zero for $x \approx 1$, we see from Fig. 15 that the polar Kerr rotation does not go to zero as the macroscopic $\mathbf{M}$ goes to zero. The polar Kerr rotation does go to zero as the spins on the individual sublattices become randomly aligned, i.e., as $x \rightarrow 2$ and $T_N \rightarrow 300°K$.

3. Two Special Cases

The dominant magneto-optical effects in systems with unpaired electrons result from the interaction between the orbital motion and the spin orientation. For our purposes we neglect the direct effect of an external magnetic field and consider only the cases with $H = 0$ and a net spin alignment. In the absence of spin-orbit interaction $\omega_e(\mathbf{v})$ and $\Gamma_e(\mathbf{v})$ are independent of $\mathbf{v}$, and since the sum over the oscillator strengths, $\sum_\nu f_{\pm e(\nu)}$, are identical, we see from Eq. (24) that $\epsilon_1 = 0$. Spin-orbit interaction enables the electron system to distinguish between the two senses of circular polarization for electric-dipole transitions—it is the physical mechanism by which the orbital electronic coordinates sense the direction of time propagation specified by the net alignment of the spin system. As mentioned above, spin-independent contributions to ϵ_1 are also found in the electric-dipole approximation and arise independently of spin-orbit interaction. However, these contributions are several orders of magnitude smaller than the ones being considered here. The two special cases described below are of particular interest for the purposes of the current investigation. In both cases linear magneto-optical effects result from spin-orbit interaction.

Case I. In the absence of spin-orbit interaction the pair of excited states $|e(\mathbf{v})\rangle = |e(\pm)\rangle$ are degenerate in energy. Spin-orbit interaction splits this degeneracy to first order in $\mathbf{M}$ by

$$\Delta E = 2\hbar\Delta\omega_e = 2\hbar(\omega_{e(+)} - \omega_{e(-)}) \quad (26)$$

but does not alter the oscillator strengths

$$f_{\pm e(\nu)} = \delta_{\pm,\nu} f_{\pm e} = \delta_{\pm,\nu} f_e, \quad (27)$$

where $\delta_{i,j} = 0$ for $i \neq j$, $\delta_{i,j} = 1$ for $i = j$, and we have taken $\Delta\omega_e \ll \frac{1}{2}(\omega_{e(+)} + \omega_{e(-)})$ in obtaining Eq. (27). The

[50] Y. R. Shen, Phys. Rev. **133**, A511 (1964).

net oscillator strengths $f_{\pm e}$ and f_e used in Eq. (27) are defined by

$$f_{\pm e} = \sum_\nu f_{\pm e(\nu)} \qquad (28)$$

and

$$f_e = \sum_\nu f_{e(\nu)}, \qquad (29)$$

where $f_{e(\nu)}$ and $f_{\pm e(\nu)}$ are defined in Eqs. (22) and (25).

Case II. In the absence of spin-orbit interaction we find equal oscillator strengths

$$f_{\pm e} = f_e \qquad (30)$$

for right and left circularly polarized transitions to the nonorbitally degenerate state $|e\rangle$. To first order in **M** the spin degeneracy of these transitions is unchanged by spin-orbit interaction, but there is a change, or splitting, of the oscillator strengths given by

$$\xi_e = (f_{-e} - f_{+e})/(f_{-e} + f_{+e}). \qquad (31)$$

Since the difference between f_{-e} and f_{+e} corresponds to a magnetic circular dichroism, we call ξ_e the fractional dichroism.

We will see in Sec. V C that electric-dipole-allowed transitions in the orthoferrites belong to case I. In addition, there are significant contributions to ε due to electric-dipole-forbidden transitions which gain intensity through the combined effects of crystal distortions and spin-orbit interaction; under certain conditions these belong to case II. While for the case-I transitions spin-orbit interaction splits the energy degeneracy of the excited states, for the case-II transitions spin-orbit interaction is quenched in the sense that it does not have nonzero diagonal matrix elements. For case II, off-diagonal matrix elements of the spin-orbit operator induce a splitting of the oscillator strengths $f_{\pm e}$ but leave the transition energies unchanged to first order in **M**. The quantitative results which follow will be used to evaluate the contributions to ε of case-I and case-II transitions.

For case I we find from Eqs. (23), (24), (26), and (27)

$$\epsilon_{1e} = -\Gamma_e \Delta\omega_e \epsilon_{0e}''_{\max}$$

$$\times \frac{(\omega - \omega_e)^2 - (\Gamma_e^2 + \Delta\omega_e^2) + 2i\Gamma_e(\omega - \omega_e)}{[(\omega - \omega_e)^2 - (\Gamma_e^2 + \Delta\omega_e^2)]^2 + 4\Gamma_e^2(\omega - \omega_e)^2}, \qquad (32)$$

where we have taken

$$\omega_e = \tfrac{1}{2}(\omega_{e(+)} + \omega_{e(-)}), \qquad (33)$$

$$\Gamma_{e(+)} = \Gamma_{e(-)} = \Gamma_e, \qquad (34)$$

and have used the identity

$$\frac{\omega - i\Gamma_e}{\omega^2 - \omega_e^2 - \Gamma_e^2 - 2i\omega\Gamma_e}$$

$$= \frac{1}{2}\left(\frac{1}{\omega_e + (\omega - i\Gamma_e)} - \frac{1}{\omega_e - (\omega - i\Gamma_e)}\right). \qquad (35)$$

In applying Eq. (35), we have considered only the effects of the resonant term $[\omega_e - (\omega - i\Gamma_e)]^{-1}$. Similarly, we find for case II

$$\epsilon_{1e} = -2\xi_e \Gamma_e \epsilon_{0e}''_{\max}$$

$$\times \frac{\omega(\omega^2 - \omega_e^2 + \Gamma_e^2) - i\Gamma_e(\omega^2 + \omega_e^2 - \Gamma_e^2)}{(\omega^2 - \omega_e^2 - \Gamma_e^2)^2 + 4\Gamma_e^2 \omega^2}. \qquad (36)$$

Equation (36) includes both resonant and nonresonant effects.

For case I, Eq. (32) shows that ϵ_{1e}' and ϵ_{1e}'' are, respectively, even and odd functions of $\omega - \omega_e$. Furthermore, for $\Delta\omega_e \ll \Gamma_e$, $\epsilon_{1e}'(\omega)$ will have a simple dissipative line shape and $\epsilon_{1e}''(\omega)$ a simple dispersive line shape. The maximum in $\epsilon_{1e}'(\omega)$ occurs for $\omega = \omega_e$ and is given by

$$\epsilon_{1e}'_{\max} = (\Delta\omega_e/\Gamma_e)\epsilon_{0e}''_{\max} \qquad (37)$$

to first order in $\Delta\omega_e/\Gamma_e$ and Γ_e/ω_e. Equation (37) is useful for calculating spin-orbit splittings $2\hbar\Delta\omega_e$ of excited states from experimental spectra.

For case II, Eq. (36) shows that ϵ_{1e}' and ϵ_{1e}'' will be, respectively, odd and even about $\omega = \omega_e$ to first order in Γ_e/ω_e. For $\Gamma_e \ll \omega_e$, $\epsilon_{1e}'(\omega)$ will have a simple dispersive shape and $\epsilon_{1e}''(\omega)$ a simple dissipative shape. These dependences are opposite to those for case I. The maximum in $\epsilon_{1e}''(\omega)$ occurs for $\omega = \omega_e$ and is given by

$$\epsilon_{1e}''_{\max} = \xi_e \epsilon_{0e}''_{\max} \qquad (38)$$

to first order in Γ_e/ω_e. This relation is useful for calculating the fractional dichroism $2\xi_e$ from experimental spectra.

In the detailed discussions of Secs. V B and V C, we show that $\xi_{\max} \lesssim (\Delta\omega/\Gamma)_{\max}$. Since case-I transitions are electric-dipole-allowed and case-II transitions are only weakly allowed, $\epsilon_0''_{\max}$ is larger for the former than for the latter. Thus, comparing Eqs. (37) and (38), we expect larger magneto-optical contributions from case-I transitions than from case-II transitions. We will see that this is substantiated by the experimental spectra.

B. Octahedral Fe^{3+} Complexes

1. Introduction

In Sec. III we found that the rare-earth orthoferrite spectra vary only slightly with different rare earths and for our current purposes can be regarded as independent of the rare earth. With the possible exception of the anomalous spectra for $SmFeO_3$ above 4.35 eV, the principal magneto-optical spectra are associated with the Fe^{3+}-O^{2-} sublattices.

Although a discussion of critical-point transitions based on an energy-band model would probably be more rigorous at higher energies, the orthoferrite spectra of the present investigation can be interpreted in terms of individual $Fe^{3+} \cdot 6O^{2-}$ molecular complexes.

The model proposed to explain the data is an extension of Clogston's original treatment of octahedrally co-ordinated Fe^{3+} ions.[9]

2. Molecular-Orbital Theory

Consider an Fe^{3+} ion octahedrally coordinated with six O^{2-} ions. Ignoring higher-order crystal-field distortions, we take the point symmetry of the ion complex to be O_h. The one-electron molecular orbitals for this octahedral ion complex are given in Fig. 17 in terms of the five $3d$, one $4s$, and three $4p$ Fe^{3+} orbits and the eighteen $2p$ O^{2-} orbits.[51,52] There are 11 one-electron energy levels of which most are degenerate, the total number of linearly independent orbital states being 27. The lowest five energy levels represent 12 bonding orbitals, which, although primarily ligand in character, do contain some admixture of cation wave functions. The two energy levels with superscript n correspond to six nonbonding orbitals, entirely ligand in nature, and the four levels with superscript $*$ are antibonding orbitals which presumably are mainly Fe^{3+} in character.

There are 41 electrons to distribute among these molecular orbitals, 36 from the ligands and 5 from the metal ion. The simplest approximation neglects electron-electron interaction effects and has the first 36 electrons completely fill the bonding and nonbonding orbitals. The last five electrons completely fill the spin-up t_{2g}^* and e_g^* orbitals, primarily Fe^{3+} ($3d$) in nature. Our insistence that the last five electrons have parallel spins results from a Hund's-rule argument which, of course, originates from electron-electron interactions. Our arguments are somewhat heuristic on this point and cannot be taken too literally. They are, nevertheless, the current arguments in the field. The high-spin Fe^{3+} ground state in the orthoferrites has been confirmed by neutron diffraction[53] and magnetization measurements.[32] Similar results show that Fe^{3+} has a high-spin ground state in the other ferric oxide compounds studied in the present investigation.[36]

The ground state for the ion complex is denoted by $^6A_{1g}$ in the Mulliken notation,[48] an orbital-singlet, spin sextuplet with even parity. Since the electric-dipole operator transforms as T_{1u} under the O_h group, the only excited states accessible by electric-dipole-allowed transitions have symmetry $^6T_{1u} = (^6A_{1g} \times T_{1u})$. The 14 one-electron electric-dipole-allowed transitions are represented by the arrows in Fig. 17. They are of two types. Twelve are charge-transfer transitions in which an electron predominantly ligand in nature is excited into an orbital predominantly Fe^{3+} in nature, e.g., the transition $t_{1u}(\sigma) \rightarrow t_{2g}^*$. Two are orbital-

[51] D. S. McClure, *Electronic Spectra of Molecules and Ions in Crystals* (Academic Press Inc., New York, 1959).

[52] J. F. Dillon, Jr., H. Kamimura, and J. P. Remeika, J. Phys. Chem. Solids **27**, 1531 (1966).

[53] W. C. Koehler, E. O. Wollan, and M. K. Wilkinson, Phys. Rev. **119**, 58 (1960).
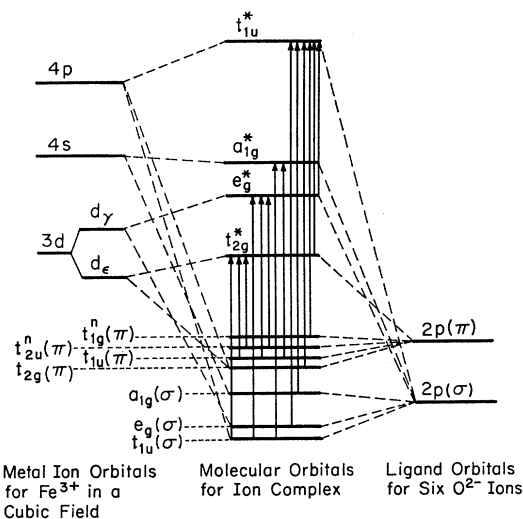
FIG. 17. Molecular orbitals for the octahedral ion complex $Fe^{3+} \cdot 6O^{2-}$ (see Refs. 51 and 52). The 14 electric-dipole-allowed transitions are given by the arrows.

promotion transitions in which an electron predominantly Fe^{3+} ($3d$) in nature is excited into an orbital predominantly Fe^{3+} ($4p$) in nature e.g., $t_{2g}^* \rightarrow t_{1u}^*$. The electric-dipole-allowed charge-transfer and orbital-promotion transitions are discussed in detail in Sec. V B 3.

In addition to the electric-dipole-allowed transitions, there are forbidden transitions which under certain conditions become weakly allowed. Of particular interest are the spin- and parity-forbidden $t_{2g}^* \rightarrow e_g^*$ crystal-field transitions considered in detail in Sec. V B 4. There are also spin-allowed and parity-forbidden charge-transfer and orbital-promotion transitions, e.g., $t_{1g}^n(\pi) \rightarrow t_{2g}^*$. These are discussed in Sec. V C.

3. Electric-Dipole-Allowed Transitions

a. Ground state. The high Néel temperatures for the ferric oxide compounds imply strong exchange fields. In the presence of a strong exchange field, the sixfold spin degeneracy of the $^6A_{1g}$ ground state is removed, and at low temperatures only the lowest-lying spin state $|^6A_{1g}, m_L=0, m_S=\frac{5}{2}\rangle$ is occupied. At room temperature a small fraction of the electron population occupies the higher-energy spin states, but it is sufficient to consider only the electrons in the lowest-lying spin state. The thermal population of the other states is negligible for qualitative purposes.

The high population at room temperature of the $m_S = \frac{5}{2}$ level is confirmed by magnetization data, e.g., the individual sublattice magnetizations for GdIG.[36] At $300°K$ the respective magnetizations of the octahedral and tetrahedral Fe^{3+} sublattices, for this example, are roughly 90 and 82% of their $0°K$ saturation values. The other ferric oxide compounds have similar higher Néel temperatures and will therefore have
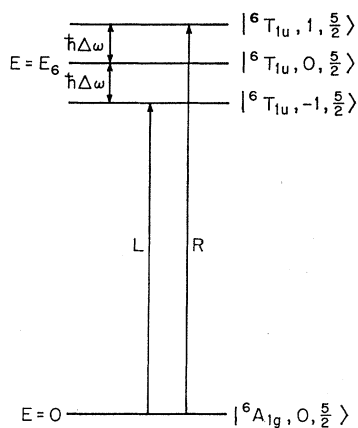
FIG. 18. Spin-orbit splitting of $|{}^6T_{1u}, m_L, \frac{5}{2}\rangle$. The left and right circularly polarized transitions L and R are for light propagation parallel to the magnetic axis.

similarly high ground-state population of $m_S = \frac{5}{2}$. Also note that in the Kerr rotation measurements on $Eu_3Fe_{5-x} Ga_x O_{12}$ (Fig. 15), no new structure appeared as the Néel points approached room temperature with increasing Ga concentration except for the weak shoulder at about 4.4 eV.

b. Excited states. We have shown that the excited states for the electric-dipole-allowed transitions have symmetry ${}^6T_{1u}$. The spin degeneracy is removed by the strong exchange field, leaving the state $|{}^6T_{1u}, m_L, \frac{5}{2}\rangle$ lying lowest in energy. We have assumed here that the effects of spin-orbit coupling and noncubic crystal fields are much smaller than those of exchange. This assumption is satisfactory for qualitative purposes.

We also assume the effects of noncubic crystal fields to be much smaller than those of spin-orbit coupling. Then the spin-orbit interaction removes the orbital degeneracy of the state $|{}^6T_{1u}, m_L, \frac{5}{2}\rangle$ as shown in Fig. 18. The states $|{}^6T_{1u}, m_L + 1, \frac{3}{2}\rangle$ are admixed with states $|{}^6T_{1u}, m_L, \frac{5}{2}\rangle$ by the spin-orbit coupling, but this admixture can also be neglected for qualitative purposes. Noncubic crystal fields partially quench the orbital magnetic moment. These can be neglected for purposes of the present discussion, but their significant effects in the orthoferrites will be considered further in Sec. V C.

c. Contributions to ε. Light propagating parallel to the magnetic axis excites the $(m_L = 0) \rightarrow (m_L = \pm 1)$ transitions L and R indicated in Fig. 18. These transitions have equal oscillator strengths but opposite senses of circular polarization and are therefore case-I transitions (Sec. V A 3). Thus the expressions derived for the contributions to ε by case-I transitions are directly applicable to the electric-dipole-allowed charge-transfer and orbital-promotion transitions. Note, in particular, that ϵ_{1e}' max, given by Eq. (37), is direct measure of the spin-orbit splittings for these allowed excitations.

In this one-electron transition approximation, the states $|{}^6T_{1u}\rangle$ are the product of wave functions of the

occupied one-electron molecular orbitals. Thus the spin-orbit splitting of $|{}^6T_{1u}\rangle$ is the sum of the spin-orbit splitting of the one-electron states of which it is composed. Spin-orbit splittings arise only for those one-electron states that have nonvanishing diagonal matrix elements of the orbital angular-momentum operator.

Since orbital angular momentum transforms as T_{1g} under O_h, the metal-ion-like orbitals a_{1g}^* and e_g^* do not have spin-orbit splittings. The bonding and nonbonding orbitals can have nonzero diagonal matrix elements of orbital angular momentum as a result of the admixture of Fe^{3+} wave functions into these orbits. If we assume this admixture to be small, these states can be taken to have negligible spin-orbit splittings. When these ligandlike orbitals overlap among themselves, electrons can circulate around the central Fe^{3+} ion by moving from O^{2-} ion to O^{2-} ion. Clogston's estimates show that even in the case of extreme overlap the maximum contribution to spin-orbit splitting from the ligandlike orbitals is about 15 cm^{-1}. This is over an order of magnitude smaller than the estimated contributions from the antibonding orbitals, 175 cm^{-1} from t_{2g}^* and 270 cm^{-1} from t_{1u}^*.[9] We conclude that only the allowed one-electron transitions to the $3d$-like t_{2g}^* and to the $4p$-like t_{1u}^* orbitals have significant spin-orbit splittings. Thus, in the absence of extreme linewidths effects, these transitions make the largest case-I contributions to ϵ_1.

For the allowed charge-transfer transitions, only the excited electrons contribute significantly to the spin-orbit splitting. However, for the allowed orbital-promotion transition $t_{2g}^* \rightarrow t_{1u}^*$, the spin-orbit splitting of the t_{2g}^* hole must be subtracted from the contribution of the t_{1u}^* excited electron. As previously indicated, the former is less than the latter; thus the contribution of the hole reduces the net spin-orbit splitting associated with the $t_{2g}^* \rightarrow t_{1u}^*$ transition but does not change its sign.

Since all the spin-up e_g^* and t_{2g}^* levels are filled for the assumed ground state, and spin is conserved for electric-dipole transitions, the electrons entering these levels in charge-transfer transitions go in with their spins reversed to that of the ferric ion. Similarly, the electrons in the t_{2g}^*, $e_g^* \rightarrow t_{1u}^*$ orbital-promotion transitions enter the excited states with their spins parallel to that of the ferric ion. Therefore the spin-orbit splittings (and ϵ_1) have opposite signs for these orbital-promotion and charge-transfer transitions. Note that charge-transfer transitions to the $4p$-like t_{1u}^* level can have either sign, depending on whether the excited electron is initially in a ligandlike spin-up or spin-down state.

The $(3d^4 4p)$ ${}^6P$-term energy of the free Fe^{3+} ion is 190 000 cm^{-1} (23.55 eV).[54] Wood and Remeika[16] find the reduced-term energies for octahedrally coordinated Fe^{3+} ions in YIG (see Sec. V B 4) to be about 64% of

[54] C. E. Moore, Natl. Bur. Std. (U. S.) Circ. **467**, Vol. II (1952).

FIG. 19. Results of crystal-field computation for Fe^{3+} (after Wood and Remeika, Ref. 16). (a) Splitting of $3d^5$ terms in octahedral (right) and tetrahedral (left) crystal fields. The vertical line gives the best fit with the observed low-lying absorption in each case (see text). (b) Summary of computed and observed energy levels, not including results of the present investigation.

the free-ion values. Assuming a similar reduction in the ^6P-term energy, we expect the lowest-energy transitions to t_{1u}^* to occur at about 15 eV. This is well beyond the range of our Kerr measurements. Therefore, of the 14 allowed electric-dipole transitions of Fig. 17, only the three charge-transfer transitions $t_{2u}{}^n(\pi)$, $t_{1u}(\pi)$, $t_{1u}(\sigma) \rightarrow t_{2g}^*$ are expected to produce significant linear magneto-optical effects within the energy range covered by the Kerr measurements.

Since $t_{1u}(\pi)$ mixes only with $t_{1u}^*(4p)$, which is expected to lie 15 eV higher in energy, it should be approximately nonbonding and almost degenerate with the nonbonding orbitals $t_{2u}{}^n(\pi)$ and $t_{1g}{}^n(\pi)$. The $\pi \rightarrow t_{2g}^*$ one-electron transitions lie about $10Dq$ lower than the $\pi \rightarrow e_g^*$ transitions. The latter, while having negligible magneto-optical effects, should be more intense than the former because of greater overlap between the ligandlike and metal-ion-like wave functions. Note that e_g^* is σ-like symmetry, while t_{2g}^* has π-like symmetry. The $t_{1u}(\sigma) \rightarrow e_g^*$ transitions is expected to have the highest intensity because of the high $t_{1u}(\sigma) - e_g^*$ overlap. Neglecting electron-electron interactions, we see from Fig. 17 that this transition has the highest energy of the allowed one-electron transitions to $3d$-like excited states. There is no evidence that this is not still true when interaction effects are included.

d. Many-electron effects. The preceding discussion has been based on one-electron transition energies and simple-product wave functions. A self-consistent many-electron treatment would account for configuration interactions resulting from the Coulomb repulsion terms (e^2/r_{ij}) and would employ wave functions symmetrized to make the electrons indistinguishable. It would result in corrections to the one-electron transition energies and other observables. Such an approach would require detailed computations beyond the scope

and purpose of the current investigation. However, it is possible to estimate the many-electron corrections resulting from intra-atomic exchange on the Fe^{3+} ions.

Dillon et al.[52] have shown that the effect of intra-atomic exchange in the Cr^{3+} ion of the chromium trihalides is to invert the energies of the transitions to e_g^* and t_{2g}^*. For example, in Cr^{3+} the transition $t_{2u}{}^n(\pi) \rightarrow t_{2g}^*$ occurs at higher energy than the transition $t_{2u}{}^n(\pi) \rightarrow e_g^*$, just the reverse of the one-electron result. The effects of intra-atomic exchange are determined in the crystal-field approximation by application of the electrostatic energy matrices for the appropriate d^n configuration.[48,51]

We find for Fe^{3+}, in contrast to the results for Cr^{3+}, that there are no intra-atomic exchange corrections for transitions to $3d$-like orbitals. The reason why important corrections occur for Cr^{3+} but not for Fe^{3+} is that in Fe^{3+} the excited electron, added to a $^6A_{1g}$ spherically symmetric d^5 shell with all the spin-up states filled, has no choice but to go in with opposite spin, whereas Cr^{3+} has the nonspherically symmetric ground state $^4A_{2g}$, and the empty e_g^* orbits can be occupied with either spin polarity. The possibility of saving in spin exchange energy exists for Cr^{+3}, but not for Fe^{+3}.

4. Crystal-Field Transitions

a. Transition energies. Spin-orbit interactions, Fe^{3+}-Fe^{3+} interactions, lattice distortions, and other effects combine to make the otherwise spin- and parity-forbidden $t_{2g}^* \rightarrow e_g^*$ transitions weakly allowed. The t_{2g}^* and e_g^* orbitals are $3d$-like orbitals localized on the Fe^{3+} ion. As a result, the many-electron states for these transitions can be considered within the framework of the crystal-field theory.[51] The transitions between

the crystal-field-split many-electron states are traditionally called crystal-field transitions.

The results of a computation by Wood and Remeika[16] for Fe^{3+} in octahedral and tetrahedral crystal fields are displayed in Fig. 19(a). The term splittings for the $3d^5$ electronic configuration are plotted as a function of the cubic crystal-field parameter Dq, where $10Dq$ is the cubic crystal-field splitting of the one-electron e_g^* and t_{2g}^* levels. Covalency effects are accounted for by the electrostatic interaction parameters B and C which result in reduced-term energies.

The lowest-lying crystal-field transitions have lower energies that the lowest-lying charge-transfer transitions. It is therefore possible to observe absorption peaks attributed to the crystal-field transitions at energies for which the ferric oxide compounds are still relatively transparent. Wood and Remeika's best fits to absorptions observed in transmission through thin samples of YIG and iron-doped yttrium gallium garnet are given by the vertical lines in Fig. 19(a) along with the best-fit values for the parameters Dq, B, and C. Figure 19(b) compares the computed crystal-field spectra with absorptions observed in garnets and orthoferrites.

The highest-energy spectra in Fig. 19(b) were observed in transmission through an yttrium gallium garnet sample doped with several atomic precent of iron. Note that even at this low iron concentration (pure yttrium gallium garnet being relatively transparent), absorption peaks were not observable in transmission beyond 26 700 cm^{-1} (3.31 eV). In Sec. V C crystal-field transitions occurring at considerably higher energies will be identified from the spectra of the present investigation.

b. Enhancement and contributions to ε. The strengths of the crystal-field transitions will be considerably enhanced when electric-dipole-allowed excitations, which can be admixed to relieve the parity constraint, lie close by in energy. The odd-parity charge-transfer excitations, discussed in Sec. V B 3, are nearly degenerate with the crystal-field excitations and thereby considerably enhance the intensity of the latter.

The exact mechanisms by which the crystal-field transitions are enhanced depends on the symmetry of the participating states. Clogston has considered in detail the enhancement of the transition $^6A_{1g}(^6S)$ $\rightarrow {}^4T_{1g}(^4G)$ by spin-orbit interaction and lattice vibrations. Assuming only the lowest spin level $|g\rangle_0$ $= |{}^6A_{1g}(^6S),0,\frac{5}{2}\rangle$ of the exchange-split $^6A_{1g}(^6S)$ crystal-field state to be occupied, he has shown that spin-orbit interaction admixes this level with $|e\rangle_0$ $= |{}^4T_{1g}(^4G),1,\frac{3}{2}\rangle$, which has also been split off by the exchange field. The new ground and excited states are given by

$$|g\rangle_1 = |{}^6A_{1g}(^6S),0,\tfrac{5}{2}\rangle + (5^{1/2}\lambda N_p/E_4)|{}^4T_{1g}(^4G),1,\tfrac{3}{2}\rangle$$

and

$$|e\rangle_1 = |{}^4T_{1g}(^4G),1,\tfrac{3}{2}\rangle$$
$$- (5^{1/2}\lambda N_p/E_4)|{}^6A_{1g}(^6S),0,\tfrac{5}{2}\rangle, \quad (39)$$

where λ is the spin-orbit coupling parameter, E_4 is the energy difference between $|g\rangle_0$ and $|e\rangle_0$, and N_p is the fractional amount of ^4P admixed with ^4G in forming $^4T_1(^4G)$. Note that these levels are coupled by spin-orbit interaction only because $^4T_1(^4G)$ has an admixture of (^4P). Reference to Fig. 19(a) shows that this admixture occurs only for states of T_1 symmetry.

In order to relieve the parity constraint, Clogston considered the admixture of $^6T_{1u}$ orbital-promotion excitations by lattice vibrations, but his approach applies equally well to $^6T_{1u}$ charge-transfer excitations admixed by either lattice vibrations or distortions. The weak temperature dependence of Dillon's absorption data for YIG[8] argues against admixture by the lattice vibration mechanism. The high ^6P-term energies for the free Fe^{3+} ion (Sec. V B 3 c) argue against orbital promotion as the source of odd-parity excitations.

Lattice distortions can result in odd-parity crystal-field terms of the form $ax+by+cz$. These odd-parity potentials admix the states $|{}^6T_{1u},m_L,\frac{5}{2}\rangle$ with the $|{}^6A_{1g}(^6S),0,\frac{5}{2}\rangle$ parts of $|g\rangle_1$ and $|e\rangle_1$ in Eq. (39). This results in a new set of wave functions, $|g\rangle_2$ and $|e\rangle_2$, which may be found in Clogston's paper. In this manner the combination of spin-orbit interaction and lattice distortion allows electric-dipole transitions to take place between $|g\rangle_2$ and $|e\rangle_2$. The right and left circularly polarized electric-dipole transitions between these two states have degenerate energies but differ in oscillator strengths. They therefore correspond to the case-II transitions of Sec. V A 3.

Using the wave functions derived by Clogston for $|g\rangle_2$ and $|e\rangle_2$, we find the oscillator strengths

$$f_{\pm e} = f_0 \left(\frac{(\sqrt{5})N_p\lambda}{E_4} \frac{|\alpha|}{E_6} \right)^2$$

$$\times \left(1 + \frac{E_6}{E_6-E_4} \pm \frac{\hbar\Delta\omega}{E_6} \frac{E_4}{E_6-E_4} \right) \quad (40)$$

for

$$1 + E_6/(E_6-E_4) \gg (\hbar\Delta\omega/E_6)[E_4/(E_6-E_4)], \quad (41)$$

where

$$E_6 = E(|{}^6T_{1u},0,\tfrac{5}{2}\rangle) - E(|{}^6A_{1g}(^6S),0,\tfrac{5}{2}\rangle),$$

$$\mp\hbar\Delta\omega = E(|{}^6T_{1u},0,\tfrac{5}{2}\rangle) - E(|{}^6T_{1u},\pm 1,\tfrac{5}{2}\rangle),$$

$$|\alpha| = |\langle {}^6A_{1g}(^6S),0,\tfrac{5}{2}|ax+by+cz|{}^6T_{1u},\pm 1,\tfrac{5}{2}\rangle|,$$

and

$$f_0 = (2m\omega_e/\hbar)|\langle {}^6A_{1g}(^6S),0,\tfrac{5}{2}|x|{}^6T_{1u},\pm 1,\tfrac{5}{2}\rangle|^2.$$

For the case in which the inequality of Eq. (41) is reversed, i.e., when $E_6 \approx \frac{1}{2}E_4$, the right-hand side of Eq. (41) should be multiplied by the factor ± 1.

Equation (40) shows that the difference in oscillator strengths for the two senses of circular polarization arises from the spin-orbit splitting $h\Delta\omega$ of the odd-parity excitation ${}^6T_{1u}$. It also demonstrates the enhancement of oscillator strength by the combined mechanisms of spin-orbit interaction, proportional to λ, and lattice distortion, proportional to $|\alpha|$. The intensity of these charge-transfer-enhanced crystal-field transitions increases as $|E_6-E_4|$ approaches zero. Note that the right-hand side of Eq. (40) becomes infinite for $E_6=E_4$ only because of the perturbation theory used in the calculation. As $E_6 \to E_4$ one should use a degenerate perturbation theory. In practice, the inclusion of linewidth effects would limit the maximum oscillator strengths.

The magneto-optical contributions of these case-II transitions are characterized by the parameter ξ, Eq. (31). We find from Eq. (40) that

$$\xi = -\frac{h\Delta\omega}{E_6}\frac{E_4}{E_6-E_4}\left(1+\frac{E_6}{E_6-E_4}\right)^{-1}, \qquad (42)$$

for the case of Eq. (41). When the inequality of Eq. (41) is reversed, the left-hand side of Eq. (42) becomes ξ^{-1}. Note that ξ depends only on the spin-orbit splitting of ${}^6T_{1u}$ and the energies of ${}^6T_{1u}$ and ${}^4T_{1g}$ relative to ${}^6A_{1g}$. Note also that as $E_6 \to \frac{1}{2}E_4$, the inequality of Eq. (41) is reversed, the left-hand side of Eq. (42) becomes ξ^{-1}, and thus $\xi \to 0$. Physically speaking, this is because the spin-orbit-split components of $|{}^6T_{1u}\rangle$ admix equally with the $|{}^6A_{1g}\rangle$ parts of $|g\rangle_1$ and $|e\rangle_1$ when $E_6=\frac{1}{2}E_4$.

C. Orthoferrite Spectra

1. Summary of Important Results of Secs. V A and V B

In Sec. V C 3, we make transition assignments for the optical and magneto-optical spectra of $EuFeO_3$ which were shown in Sec. III to be characteristic of all the orthoferrites. Before proceeding, we summarize briefly some of the important results of Secs. V A and V B which we will use in making these identifications.

In Sec. V A we derived an expression relating the oscillator strength to $\epsilon_{0e}''_{max}$ for Lorentzian lines. We also distinguished between the contributions to ϵ_1 of case-I and case-II transitions, defined in Sec. V A. Case-I and case-II transitions have, respectively, dissipative and dispersive shaped contributions to $\epsilon_1'(\omega)$ and can be described respectively by the spin-orbit splitting $\Delta\omega$ and the fractional dichroism ξ. The spin-orbit splitting is related to $\epsilon_1'_{max}$ by Eq. (37), and the fractional dichroism to $\epsilon_1''_{max}$ by Eq. (38).

In Sec. V B, we showed that the characteristic optical resonances for $Fe^{3+}\cdot 6O^{2-}$ octahedra can be described in terms of a molecular-orbital model. The electric-dipole-allowed transitions correspond to charge transfer or orbital promotion. There are also electric-dipole-forbidden crystal-field transitions whose in-
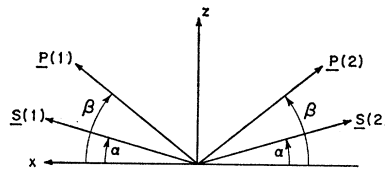

FIG. 20. System with two magnetic sublattices. Spins $S(1)$ and $S(2)$ and principal axes $P(1)$ and $P(2)$ lie in xz plane.

tensities are enhanced by nearby odd-parity excitations such as charge transfer.

The electric-dipole-allowed transitions were shown to be case-I excitations. The six allowed charge-transfer transitions to $t_{2g}{}^*$ and $e_g{}^*$ are expected to lie lowest in energy with the transitions to $t_{2g}{}^*$ having the largest magneto-optical effects and the transitions to $e_g{}^*$ the strongest intensity.

The crystal-field transitions derive their intensity from a variety of mechanisms. We considered in detail the ${}^6A_{1g}({}^6S) \to {}^4T_{1g}({}^4G)$ transitions and showed that a case-II description is appropriate when this transition is enhanced by the combined effects of spin-orbit coupling and lattice distortions.

2. Effects of Spin Canting and Site Symmetry

We have shown in Sec. II that linear magneto-optical effects originate in the antisymmetric part of the dielectric tensor. In that discussion we assumed only ϵ_{xy} to be nonzero. In the most general case, ϵ_{yz} and ϵ_{zx} are also nonzero, and the antisymmetric part of $\boldsymbol{\epsilon}$ may be represented by the pseudovector $\mathbf{V}$:

$$V_l = \frac{1}{2}\sum_{jk}\epsilon_{jkl}\epsilon_{jk}, \qquad (43)$$

where ϵ_{jkl} is the alternating tensor and ϵ_{jk} is the jk element of the dielectric tensor. Note that $V_z = i\epsilon_1$ in this notation.

For a system with noninteracting magnetic sublattices, we may take

$$\mathbf{V} = \frac{1}{2}\sum_{m}\boldsymbol{\Gamma}(m)\cdot\mathbf{S}(m), \qquad (44)$$

where $\mathbf{S}(m)$ is the spin of the mth sublattice. Observe from Eq. (44) that the magnitude and orientation of $\mathbf{V}$ depends on both the magnitudes and orientations of $\mathbf{S}(m)$ and the magnitudes and principal axes of $\boldsymbol{\Gamma}(m)$.

For example, consider a two-sublattice system in which the spins $\mathbf{S}(m)$ and principal axes $\mathbf{P}(m)$ are located in the xz plane at the angles specified in Fig. 20. For simplicity assume that $|\mathbf{S}(1)| = |\mathbf{S}(2)| = S$ and that the only nonzero components of $\boldsymbol{\Gamma}(m)$ are $\Gamma_{z'z'}(m) = \gamma$, where z' is taken along $\mathbf{P}(1)$ and $\mathbf{P}(2)$ for the respective sublattices. We then find from Eq. (44) that

$$V_z = \gamma S[\cos(\beta-\alpha)]\sin\beta = g(\alpha,\beta)\gamma S. \qquad (45)$$

We observe from Eq. (45) that the linear magneto-optical effects are proportional to the sine of the canting

TABLE II. Summary of transition assignments including energies (E), oscillator strengths (f), linewidths (2Γ), tensor elements (ϵ_0'') and $\epsilon_1')$, spin-orbit splittings $(2\Delta\omega)$, and comparisons with estimated or calculated values where available.

	Charge-transfer transitions	E_{expt} (eV)	$2\Gamma_{e\,\text{expt}}$ (eV)	$\epsilon_{1e}''_{\text{max expt}}$	$\epsilon_{1e}'_{\text{max expt}}$	$f_{e\,\text{expt}}$	$(2g_e\Delta\omega_e)_{\text{expt}}$[a] (cm^{-1})	$f_{e\,\text{expt}}$[b]	$2\Delta\omega_{e\,\text{est}}$[b] (cm^{-1})
(A)	$t_{2u}{}^n(\pi) \rightarrow t_{2g}{}^*$	3.0	0.5	0.85	0.023	0.05	109	0.13	175
(B)	$t_{1u}(\pi) \rightarrow t_{2g}{}^*$	3.15	0.9	2.24	0.013	0.27	42	0.13	175
(C)	$t_{1u}(\sigma) \rightarrow t_{2g}{}^*$	3.85	0.3	4.18	0.044	0.20	25	0.13	175
(D)	$t_{2u}{}^n(\pi) \rightarrow e_g{}^*$	4.25	0.6	4.46	<0.004	0.47	<4.5	<0.40	<15
(E)	$t_{1u}(\pi) \rightarrow e_g{}^*$	4.70	0.4	2.35	<0.001	0.18	<1.5	<0.40	<15
(F)	$t_{1u}(\sigma) \rightarrow e_g{}^*$	$\sim$5.25						<0.40	<15

	Charge-transfer-enhanced crystal-field transitions	E_{expt} (eV)	E_{calc}[c] (eV)
(a)	$^6A_{1g}(^6S) \rightarrow {}^4E_g(^4G),\, ^4A_{1g}(^4G)$	2.35	2.49
(b)	$^6A_{1g}(^6S) \rightarrow {}^4T_{2g}(^4D)$	2.68	2.76
(c)	$^6A_{1g}(^6S) \rightarrow {}^4E_g(^4P)$		3.10
(d)	$^6A_{1g}(^6S) \rightarrow {}^4T_{1g}(^4P)$	3.60	3.70
(e)	$^6A_{1g}(^6S) \rightarrow {}^4A_{2g}(^4F)$	4.10	4.12
(f)	$^6A_{1g}(^6S) \rightarrow {}^4T_{1g}(^4F)$	4.40	4.57

[a] Canted antiferromagnetic alignment and anisotropic orbital quenching is accounted for by g_e (see text).
[b] See Ref. 9.
[c] See Ref. 16.

angle α for $\beta=90°$. Similarly, if the site symmetry of the magnetic ions were cubic, $\boldsymbol{\Gamma}(m)$ would be a diagonal tensor, and V_z would be proportional to $\sin\alpha$. Anisotropy in $\boldsymbol{\Gamma}(m)$ enables the spin components $S_x(m)$ and $S_y(m)$ as well as $S_z(m)$, to contribute to the magneto-optical effects.

This anisotropic mechanism appears to be particularly significant in the orthoferrites where the magnitude of the spin component in the xy plane is about 125 times $S_z(m)$ and where the $\bar{1}$ site symmetry of the Fe^{3+} ions implies large anisotropy. The tensor $\boldsymbol{\Gamma}(m)$ is a function of the orbital angular momentum, and it is therefore appropriate to give the name anisotropic orbital quenching to this mechanism, which we believe is responsible for enhancement of the linear magneto-optical effects in the orthoferrites. Anisotropic quenching explains why the observed Kerr rotations in the orthoferrites are of the same magnitude as those in the ferrimagnetic ferric oxide compounds, even though the latter have net magnetizations an order of magnitude larger. Note that in the ferrimagnetic systems the spin components $S_z(m)$ are quite large, and anisotropic orbital quenching need not be considered in order to explain the large magneto-optical effects observed.

Equations (37) and (38) may be rewritten as

$$\epsilon_{1e}'_{\text{max}} = (g_e\Delta\omega_e/\Gamma_e)\epsilon_{0e}''_{\text{max}} \qquad (46)$$

and

$$\epsilon_{1e}''_{\text{max}} = g_e\xi_e\epsilon_{0e}''_{\text{max}}, \qquad (47)$$

where the factor g_e has been added to account for the combined effects of spin canting and antisotropic orbital quenching. Experimentally, we find in Sec. V C 3 that g_e is of order unity. Calculation of g_e would require a detailed molecular-orbital treatment accounting for the symmetries of the Fe^{3+} sites.

We observe that anisotropy in the symmetric part of $\boldsymbol{\varepsilon}$ will in general accompany the anisotropy in the antisymmetric part. However, this is of no consequence to the present discussion because we have already shown in Sec. II C that pleochroism, originating in the symmetric part of $\boldsymbol{\varepsilon}$, does not quench the linear magneto-optical effects. The expected sensitivity of g_e to lattice distortions and detailed properties of the molecular orbitals is a likely origin of the small variations observed in the magneto-optical spectra for ferric oxide compounds with different rare-earth ions.

A simple physical example by which anisotropic orbital quenching can be understood is obtained by adding the effects of a large axial crystal field to the energy-level diagram shown in Fig. 18. This has the effect of lifting the near degeneracy of the three $m_e=0$, ± 1 states. One can then demonstrate that near the resonance frequency $\hbar\omega\approx E_6$, the axial field quenches the orbital angular momentum such that only $\Gamma_{z'z'}$ remains large. The z' direction is the direction of the axial crystal field. This quenching effect is no longer appreciable for $|\hbar\omega - E_6|$ large compared to the axial field energy. This very likely contributes to the sharpness of the observed magneto-optical structure in the orthoferrites.

3. Transition Assignments

Assuming the Lorentzian line shapes of Eqs. (21) and (24), the observed $\epsilon_1'(\omega)$ and $\epsilon_0''(\omega)$ can be explained by the transition assignments and associated parameters listed in Table II. The good agreement between the assignments and experiment is indicated by the theoretical curves of Fig. 21· where the contributions of charge-transfer transitions (A)-(C) to $\epsilon_1'(\omega)$ and (A)-(E) to $\epsilon_0''(\omega)$ are compared with the experimental spectra. The fit could undoubtedly be improved by
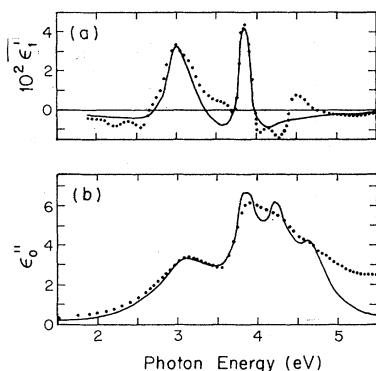
Photon Energy (eV)

FIG. 21. Comparison of experimental and theoretical dielectric-tensor components for EuFeO$_3$. (a) Experimental off-diagonal element ϵ_1' (points) compared with theoretical contribution (solid line) from charge-transfer transitions (A)-(C). (b) Experimental diagonal element ϵ_0'' (points) compared with theoretical contribution (solid line) from charge-transfer transitions (A)-(E).

further computation, but the present agreement is most satisfactory. The validity of the crystal-field transition assignments is supported by the good agreement with the energies obtained from the crystal-field computation of Wood and Remeika.[16]

One of the most important results of the present investigation is the observation, through the magneto-optical effects, of unresolved structure in the straight reflectivity spectra. Note, for example, charge-transfer transitions (A) and (C) and crystal-field transition (f).

The strong magneto-optical peak in ϵ_1' at 3.0 eV, corresponding to (A), is unresolved in ϵ_0'', and the strong peak in ϵ_0'', corresponding to (B), appears as a shoulder in ϵ_1'. Although transition (C) contributes a peak in ϵ_0'' at 3.90 eV associated with a strong but broad absorption, its relatively narrow linewidth is apparent only from the width of the peak in ϵ_1' at 3.58 eV. The linewidth of this case-I transition is determined from Eq. (32), which shows that $\epsilon_{1e}' = 0$ for $\omega = \omega_e \pm \Gamma_e$ to first order in $\Delta\omega_e/\Gamma_e$.

Except for (b), none of the magneto-optically resolved crystal-field transitions is resolved in the straight optical data. The dispersive structure in ϵ_1' at 4.40 eV identifies (f) as a charge-transfer-enhanced crystal-field transition. The dispersive shapes in ϵ_1' of the other crystal-field transitions are not as obvious. Note that we have only shown that the crystal-field transitions $^6A_{1g} \rightarrow {}^4T_{1g}$ belong to case II. Although the detailed line shapes resulting from the other crystal-field transitions require further theoretical investigation, we believe that this is a general characteristic of crystal-field transitions. The other transitions were thus identified largely from their dissipative-shaped contributions to ϵ_1''. Once all the energies at which crystal-field transitions occur were determined, the individual transitions were identified by comparison with the computed results of Wood and Remeika (Fig. 19). Note that (f), the best-resolved crystal-field transition,

is a $^6A_{1g} \rightarrow {}^4T_{1g}$ excitation, the type discussed in detail in Sec. V B.

The proposed assignments are self-consistent but not unique. For example, an alternative interpretation of these spectra would assign transitions (A) and (B) as degenerate in energy at 3.15 eV and would account for the peak in ϵ_1' at 3.00 eV by crystal-field transition (c), or vice versa with (A) and (B) at 3.00 eV and (c) at 3.15 eV. Further discussion of these fine points is not justified in the absence of detailed molecular-orbital calculations.

While the spectra for EuFeO$_3$ are characteristic of all the rare-earth orthoferrites, the observed charge-transfer and crystal-field transitions show small but interesting variations in ϵ_1 with different rare earths. We quote here several examples.

(1) Transition (B), which contributes only weak shoulders in ϵ_1' (Fig. 6) for the orthoferrites with light rare earths (Eu, Sm, Tb), contributes better-defined peaks for the intermediate-weight orthoferrites (Dy and Y) and well-resolved peaks for the heavy orthoferrites (Tm and Lu).

(2) Transition (a) tends to occur at higher energies for orthoferrites with lower-atomic-number rare earths (Fig. 3). Note from Fig. 19 that both the ground and excited states for this transition are independent of Dq. However, the variation in transition energy with different rare earths could perhaps be attributed to variations in the ^6S-^4G term separation.

(3) Transition (a) is apparently split into two peaks at 2.234 and 2.275 eV for YbFeO$_3$ (Fig. 3).

(4) Transitions (e) and (f) are resolved best in ϵ_1'' for YFeO$_3$ (Fig. 6). They are found at 4.0 and 4.45 eV, respectively, in this material.

4. Spin-Orbit Splitting

The experimental values in Table II for $2g_e\Delta\omega_e$, the spin-orbit splittings reduced to account for the combined effects of the canted antiferromagnetic alignment and anisotropic orbital quenching, are much larger for the excited states of charge-transfer transitions (A)-(C) than for those of (D) and (E). This result aided in making the transition assignments.

The absolute values for $2\Delta\omega_e$ agree with Clogston's estimates when $g_e \approx \frac{1}{2}$. This could be explained only by considerable anisotropic orbital quenching in the ortho-ferrites, resulting in a highly anisotropic $\Gamma(m)$ [Eq. (44)]. In the absence of anistropic quenching, $g_e = \sin\alpha$ for the two-sublattice model of Fig. 20. Since $\sin\alpha \approx 0.008$ for the orthoferrites,[32] the resulting values for $\Delta\omega_e$ expt would be two orders of magnitude too large. For ferrimagnetic ferric oxide compounds such as YIG, experimental values for ϵ_1' (Fig. 13) are of the same order of magnitude as for the orthoferrites. For these ferrimagnetic materials $\sin\alpha = 1$, and $2g_e\Delta\omega_e$ agrees with Clogston's estimates in the absence of anisotropic quenching.

The effects of anisotropic quenching are qualitatively significant only in materials with sublattice magnetizations orders of magnitude larger than the net magnetization. Thus, of the materials investigated, it is only in the orthoferrites that anisotropic quenching plays a qualitative role.

5. Fractional Dichroism

Spin-orbit splittings were also determined from the observed fractional dichroisms attributed to charge-transfer-enhanced crystal-field transitions. Equation (42) shows that the largest fractional dichroisms occur when crystal-field transitions are nearly degenerate with allowed charge-transfer excitations, i.e., $E_6 \approx E_4$. For this limiting case, Eq. (42) becomes

$$\xi \approx -\hbar\Delta\omega/E_6 \approx -\hbar\Delta\omega/E_4. \tag{48}$$

Combining Eqs. (47) and (48), we obtain

$$g_e\hbar\Delta\omega_e \approx -(\epsilon_{1e}''_{\max}/\epsilon_{0e}''_{\max})E_4. \tag{49}$$

For transition (f), $^6A_{1g}(^6S) \rightarrow {}^4T_{1g}(^4F)$, at $E_4 = 4.4$ eV, we find $\epsilon_{1e}''_{\max} \approx -2 \times 10^{-2}$ and $\epsilon_{0e}''_{\max} < 5.0$ from Figs. 5(a) and 6(b). Insertion of these values in Eq. (49) gives $2g_e\Delta\omega_e > 284$ cm^{-1}. This result is compatible with Clogston's estimates for $g_e \gtrsim 0.8$.

In order to obtain a reasonable value for g_e we have had to assume $\epsilon_{0e}'' \sim 5$ for crystal-field transition (f). This would imply an unreasonably large oscillator strength for this allegedly weakly allowed transition. More detailed theoretical investigations are called for.

In order to provide an over-all best fit for the experimental data it would be necessary to attribute part of ϵ_0'' to the crystal-field transitions and part to the charge-transfer transitions. But in the assignments of Table II we have assumed that only charge-transfer processes contribute to ϵ_0''. However, as has been previously emphasized, these assignments are intended to be qualitative and to point the way for more detailed molecular-orbital calculations. In the absence of such calculations, further refinements of the transition assignments is not justified.

6. Parity-Forbidden Charge-Transfer Transitions

The assignments of Table II neglect the possibility of exciting spin-allowed but parity-forbidden charge-transfer transitions such as the one-electron transition $t_{1g}{}^n(\pi) \rightarrow t_{2g}^*$. These transitions, which were similarly neglected by Clogston, are weakly allowed by admixture with odd-parity charge-transfer excitations and may have intensities greater than or equal to those of the charge-transfer-enhanced crystal-field transitions. They are most intense when nearly degenerate with the allowed charge-transfer excitations.

Since they are transitions to orbitally degenerate excited states, their magneto-optical contributions have case-I symmetry and are indistinguishable by symmetry from those of the parity-allowed transitions. Thus the net effect of parity-forbidden charge-transfer transitions is to broaden and enhance the optical and magneto-optical contributions of the parity-allowed excitations. It was therefore permissible to neglect the parity-forbidden transitions in making the transition assignments. However, any detailed molecular-orbital calculations for the ferric oxide compounds should account for their contributions. Note that the theoretical curve for ϵ_0'' in Fig. 21(b) would be smoothed out by the contributions of these transitions. In accordance with our discussion of parity-allowed charge transfer, the transitions $t_{1g}{}^n(\pi)$, $t_{2g}(\pi)$, $a_{1g}(\sigma)$, $e_g(\sigma) \rightarrow t_{2g}^*$ should give the largest magneto-optical contributions to ϵ_1, while the transitions to e_g^* should make the largest contributions to ϵ_0''.

D. Ferrimagnetic Spectra

It was shown in Sec. IV that a common feature of ferrimagnetic ferric oxide compounds is tetrahedrally coordinated Fe^{3+} ions which together with the octahedrally coordinated Fe^{3+} ions provide the principal contributions to the magneto-optical spectra. While the electronic energy levels for the $Fe^{3+}{}_{\text{tet}}$ and $Fe^{3+}{}_{\text{oct}}$ molecular complexes are similar, they differ in several important respects, which we discuss below.[51]

Because of the absence of a center of inversion in the tetrahedral complexes, the wave functions are no longer states of definite parity. However, the spin constraint on electric-dipole transitions remains. The relaxation of the parity constraint results in theoretically calculated intensities for the tetrahedral crystal-field transitions at least an order of magnitude larger than for the same transitions in the octahedral complexes.[16] Observed crystal-field transition intensities are typically 100 times larger in tetrahedral than in octahedral systems.[51]

Similarly, the absence of a center of inversion implies that the charge-transfer transitions forbidden by parity in the octahedral complexes will be allowed in the tetrahedral complexes. Thus there are more charge-transfer transitions with allowed intensities associated with $Fe^{3+}{}_{\text{tet}}$ than with $Fe^{3+}{}_{\text{oct}}$. This, in combination with increased intensity of the crystal-field transitions, would explain why most of the magneto-optical structure for the garnet $Eu_3 Fe_{5-x} Ga_x O_{12}$ was experimentally observed to be associated with tetrahedral sites.

The magneto-optical contributions of the charge-transfer transitions will have case-I symmetry for the tetrahedral as well as the octahedral complexes. Because of the multiplicity of possible octahedral and tetrahedral transitions, with one notable exception it is not possible at this time to make definite assignments. The transition assignments for the orthoferrites show that only one charge-transfer transition associated with $Fe^{3+}{}_{\text{oct}}$ contributes significantly to ϵ_1 in the uv. We therefore identify the 4.17-eV peak in ϵ_1' for YIG with this $t_{1u}(\sigma) \rightarrow t_{2g}^*$ charge-transfer excitation. On

the basis of its intensity, the 4.97-eV peak in ϵ_1', previously attributed to the Fe^{3+}_{tet} complexes, is also attributed to charge transfer.

Similarly, the principal magneto-optical spectra in the other ferrimagnetic ferric oxide compounds, which occur at about the same energies as in the garnets, are attributed to the same charge-transfer processes. We conclude that charge-transfer transitions occurring at about 4 and 5 eV and associated with Fe^{3+}_{oct} and Fe^{3+}_{tet} complexes, respectively, are responsible for the principal magneto-optical spectra in all the ferric oxide compounds investigated.

VI. DISCUSSION AND SUGGESTIONS FOR FUTURE RESEARCH

A. Introduction

The current investigation has demonstrated that important information can be learned from the application of uv, magneto-optical reflection techniques. We have observed spectra for ferric oxide compounds above the visible absorption edge and have used this information to interpret the electronic structure of these scientifically and technologically important materials. Our results indicate that further study of the ferric oxide compounds and uv magneto-optical investigations of other classes of materials would be profitable. Some possible areas for further research are discussed below.

B. Ferric Oxide Compounds

1. Fe^{3+}-Fe^{3+} Interactions

A question of fundamental importance, highlighted by the results of the present investigation, is the dependence on iron concentration of the optical resonances observed in the ferric oxide compounds. From the transition assignments of Table II, we find a net oscillator strength greater than 1.2 for the iron-associated absorptions between 0 and 5 eV in the orthoferrites. However, the transmission spectra of Wood for the dilute system aluminum oxide plus 0.005-at.% iron show a net oscillator strength less than 0.1 for the octahedrally coordinated Fe^{3+} ions in the same energy range.[9] It therefore appears that the oscillator strengths of the allowed transitions in the orthoferrites are concentration-dependent.

This result is consistent with the transmission data of Wood and Remeika[16] for gallium-doped YIG. They observe absorption coefficients which are "very roughly" proportional to the square of the fraction of Fe^{3+} ions present for iron concentrations between 2 and 100 at.%. Wood and Remeika note that this quadratic dependence implies absorptions which are more characteristic of Fe-O-Fe molecules than of individual Fe^{3+} ions.

Wickersheim and Lefever[12] have argued that frequency shifts of the strong absorptions result when the

rare-earth iron garnets are diluted with gallium. The polar Kerr rotation spectra displayed in Fig. 15 for the gallium-doped garnet system Eu_3 Fe_{5-x} Ga_x O_{12} show that the transition frequencies are independent of the iron (gallium) concentration for gallium concentrations as high as 38 at.% ($x = 1.9$). We expect that this result will hold true for higher concentrations as well.

More detailed measurements on substituted ferric oxide compounds are called for and should be analyzed quantitatively to distinguish the concentration-dependent effects from the magnetization-dependent ones. Low-temperature measurements would permit investigation of garnet samples with higher gallium concentrations. Experimental investigations on substituted orthoferrites are also desirable because the orthoferrites have only Fe^{3+}_{oct} sites.

2. Theory

In order to account for the observed concentration dependence of the ocillator strengths, the molecular-orbital theories of Sec. V should be extended to consider interactions between nearest-neighbor $Fe^{3+} \cdot 6O^{2-}$ complexes. More detailed molecular-orbital calculations are also required to elaborate on the anisotropic orbital quenching mechanism. In Sec. V this mechanism was suggested as the origin of the enhanced magneto-optical effects in the orthoferrites. Similar enhancements are to be expected for other materials which are weakly ferromagnetic as a result of canted spin configurations (see Sec. VI C). More refined calculations should also be undertaken in order to elaborate on the transition assignments for the orthoferrites.

3. Additional Experiments

The room-temperature experiments on the ferrimagnetic ferric oxide compounds should be extended. Complex polar Kerr rotations, normal reflectivities, and dielectric-tensor elements should be obtained for additional materials. These results would permit further identification of the spectra for the garnets, spinel ferrites, and hexagonal compounds. The contributions of the M^{2+} ions in the spinel ferrites are of particular interest. Further studies of the influence of the rare-earth ions on the garnet spectra are desirable.

The utility of low-temperature measurements has been noted above in the discussion of concentration-dependent effects. Low-temperature measurements are also desirable on undiluted systems. Low temperatures would permit further resolution of the effects observed at room temperature and would provide access to the anisotropy-change regions of the orthoferrites. The term "anisotropy-change region" refers to the temperature range over which the easy axes of a number of orthoferrites change from [100] to [001] with increasing temperature.[31] Experimental studies in the anisotropy-change regions could provide further in-

sight into the anisotropic orbital quenching mechanism. Note that only $SmFeO_3$ undergoes a change in anisotropy above room temperature (centered about 175°C).

C. Other Materials

The magneto-optical techniques applied to the ferric oxide compounds should provide similarly important information about other materials as well. Although reflection magneto-optics is useful for studying materials which are not magnetically ordered,[55] it is most appropriate for investigating systems in which the combination of net spin alignment and substantial spin-orbit interaction results in relatively large linear magneto-optical effects, i.e., for ferri- or ferromagnetic crystals.

At room temperature, the ordered materials to which uv Kerr techniques (polar, transverse, or longitudinal) are applicable include the transition metals Fe, Co, and Ni and more complex systems such as MnBi. At low temperatures, materials which could be studied include the rare-earth metals, the chalcogenides, and the chromium trihalides. Note that the large spin-orbit coupling constants of the ligand ions in the chalcogenides and trihalides can result in large magneto-optical effects.[52] As a result these systems are of particular technological and scientific interest. Further information about anisotropic orbital quenching would be obtained from studies of additional, weakly ferromagnetic systems, such as α-Fe_2O_3, $MnCO_3$, $CoCO_3$, $Mn(C_2H_3O_2)_2 \cdot 4H_2O$, $KMnF_3$, CrF_3, the rare-earth chromites ($RCrO_3$), and the rare-earth manganites.[56,57]

ACKNOWLEDGMENTS

The authors wish to thank Dr. N. Bertram, R. Bartkowski, and Professor R. V. Jones for providing several of the samples; E. M. Kelly for assistance in crystal growth; L. Ladd and Professor W. Paul for assistance with the straight reflectivity measurements; Miss I. Rivera-Veve for programming assistance; and Dr. P. M. Grant of IBM, San Jose, Calif., for use of his Kramers-Kronig programs. The assistance and discussion of numerous other colleagues are not specified but are nevertheless gratefully acknowledged. One of the authors (F. J. K.) thanks Nippon Electric Co.,

[55] E. A. Stern, in *Optical Properties and Electronic Structure of Metals and Alloys*, edited by F. Abeles (Wiley-Interscience, Inc., New York, 1966), p. 599.

[56] A. H. Morrish, *The Physical Principles of Magnetism* (John Wiley & Sons, Inc., New York, 1965), p. 481.

[57] R. Aleonard, R. Pauthenet, J. P. Rebouillat, and C. Veyret, J. Appl. Phys. **39**, 379 (1968).

Ltd., for providing time and facilities for completion of the final version of this manuscript.

APPENDIX: DERIVATION OF COMPLEX POLAR KERR EFFECT FOR A PLEOCHROIC MEDIUM

The results discussed in Sec. II C are derived in this appendix. As has been previously emphasized, the major complication of this derivation is the nonorthogonality of the normal propagation modes.

Consider the normally incident beam of Eq. (9) and rewrite it in terms of the normal modes of Eq. (4):

$$\mathbf{E}_{in} = E_+ \hat{r}_+ + E_- \hat{r}_-. \tag{A1}$$

The modes of Eq. (4) have been normalized to give

$$\hat{r}_\pm \cdot \hat{r}_\pm{}^* = 1. \tag{A2}$$

Projecting $\mathbf{E}_{in}$ on $r_\pm{}^*$ and using Eqs. (A2) and (5), we obtain a set of linear equations which can be solved to get

$$E_\pm = (1+\gamma^2)^{-1}(\mathbf{E}_{in} \cdot \hat{r}_\pm{}^* - i\gamma \mathbf{E}_{in} \cdot \hat{r}_\mp{}^*). \tag{A3}$$

We then insert $\mathbf{E}_{in}$ and $\hat{r}_\pm{}^*$:

$$E_+ = E_0(1+\gamma^2)^{-1}$$
$$\times [i(b^* - \gamma a^*) \cos\alpha + (a^* + \gamma b^*) \sin\alpha],$$
$$E_- = E_0(1+\gamma^2)^{-1} \tag{A4}$$
$$\times [(a^* + \gamma b^*) \cos\alpha + i(b^* - \gamma a^*) \sin\alpha].$$

The reflected beam will then be

$$\mathbf{E}_r = r_+ E_+ \hat{r}_+ + r_- E_- \hat{r}_-, \tag{A5}$$

where $r_\pm$ are the appropriate reflection coefficients.

We now define a new reference frame

$$\hat{r}_\alpha = \hat{x} \cos\alpha + \hat{y} \sin\alpha,$$
$$\hat{r}_{\bar\alpha} = -\hat{x} \sin\alpha + \hat{y} \cos\alpha. \tag{A6}$$

The $\hat{r}_\alpha$ direction is parallel to the plane of polarization of $\mathbf{E}_{in}$ and the $\hat{r}_{\bar\alpha}$ direction is perpendicular to it. The reflected beam $\mathbf{E}_r$ can be rewritten in the form

$$\mathbf{E}_r = E_\alpha [\hat{r}_\alpha + (E_{\bar\alpha}/E_\alpha)\hat{r}_{\bar\alpha}], \tag{A7}$$

from which we see that the complex polar Kerr rotation will be given by

$$\Phi = E_{\bar\alpha}/E_\alpha \tag{A8}$$

for $|E_{\bar\alpha}/E_\alpha| \ll 1$. The quantities E_α and $E_{\bar\alpha}$, and hence Φ, are readily found by projecting $\mathbf{E}_r$ of Eq. (A5) on $\hat{r}_\alpha$ and $\hat{r}_{\bar\alpha}$ of Eq. (A6). Some algebra then leads to the final result given by Eq. (10).